JACS
JOURNAL OF THE AMERICAN CHEMICAL SOCIETY
ARTICLE
pubs.acs.org/JACS

Optimizing Sensitization Processes in Dinuclear Luminescent Lanthanide Oligomers: Selection of Rigid Aromatic Spacers

Jean-François Lemonnier,[§] Laure Guénée,[⊥] César Beuchat,[#] Tomasz A. Wesolowski,[*,#] Prasun Mukherjee,[‡] David H. Waldeck,[*,‡] Kristy A. Gogick,[‡,†] Stéphane Petoud,[*,‡,†] and Claude Piguet[*,§]

[§]Department of Inorganic, Analytical and Applied Chemistry and [#]Department of Physical Chemistry, University of Geneva, 30 quai E. Ansermet, CH-1211 Geneva 4, Switzerland

[⊥]Laboratory of Crystallography, University of Geneva, 24 quai E. Ansermet, CH-1211 Geneva 4, Switzerland

[‡]Department of Chemistry, University of Pittsburgh, 219 Parkman Avenue, Pittsburgh, Pennsylvania 15260, United States

[†]Centre de Biophysique Moléculaire, CNRS UPR 4301, Rue Charles-Sadron, 45071 Orléans Cedex 2, France

Supporting Information

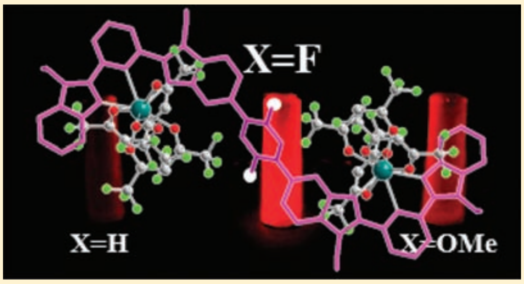

ABSTRACT: This work illustrates a simple approach for optimizing the lanthanide luminescence in molecular dinuclear lanthanide complexes and identifies a particular multidentate europium complex as the best candidate for further incorporation into polymeric materials. The central phenyl ring in the bis-tridentate model ligands **L3**−**L5**, which are substituted with neutral (X = H, **L3**), electron-withdrawing (X = F, **L4**), or electron-donating (X = OCH_3, **L5**) groups, separates the 2,6-bis(benzimidazol-2-yl)pyridine binding units of linear oligomeric multi-tridentate ligand strands that are designed for the complexation of luminescent trivalent lanthanides, Ln(III). Reactions of **L3**−**L5** with $[Ln(hfac)_3(diglyme)]$ ($hfac^-$ is the hexafluoroacetylacetonate anion) produce saturated single-stranded dumbbell-shaped complexes $[Ln_2(\mathbf{L}k)(hfac)_6]$ ($k = 3-5$), in which the lanthanide ions of the two nine-coordinate neutral $[N_3Ln(hfac)_3]$ units are separated by 12−14 Å. The thermodynamic affinities of $[Ln(hfac)_3]$ for the tridentate binding sites in **L3**−**L5** are average ($6.6 \le \log(\beta_{2,1}^{Y,\mathbf{L}k}) \le 8.4$) but still result in 15−30% dissociation at millimolar concentrations in acetonitrile. In addition to the empirical solubility trend found in organic solvents (**L4** > **L3** ≫ **L5**), which suggests that the 1,4-difluorophenyl spacer in **L4** is preferable, we have developed a novel tool for deciphering the photophysical sensitization processes operating in $[Eu_2(\mathbf{L}k)(hfac)_6]$. A simple interpretation of the complete set of rate constants characterizing the energy migration mechanisms provides straightforward objective criteria for the selection of $[Eu_2(\mathbf{L4})(hfac)_6]$ as the most promising building block.

INTRODUCTION

Beyond the now routine dispersion of luminescent trivalent lanthanides, Ln(III), into coordination polymers or hybrid materials for the production of improved dyes for organic light-emitting diodes (OLEDs) or lighting devices,[1,2] an emerging strategy is to exploit well-identified organic polymeric scaffolds for the selective sequestration of luminescent trivalent lanthanides.[3,4] In this context, specific binding sites coded for trivalent lanthanides, such as 2,2′;6′,2″ terpyridine,[3a,b,f] 1,4,7,10-tetraazacyclododecane-1,4,7,10-tetraacetic acid (DOTA),[3c] diethylenetriaminepentaacetic acid (DTPA),[3d] or propionic acid,[3e] are connected to the backbone of preformed polymers via flexible alkyl linkers (Figure 1a, type I). However, the final distribution of bound metal ions has evaded satisfactory supramolecular control.[3] Alternatively, didentate 1,10-phenanthroline[4a] or tridentate 2,6-bis(2-thienyl)pyridine[4b] chelates can be incorporated within the backbone of the organic polymers with the aim of improving structural control over metal ion placement upon complexation (Figure 1b, type II).

Alhough structural and thermodynamic data for metal loading in these type II polymers are still scarce,[4] Borkovec and co-workers theoretically predicted that, depending on the sign of the pair interaction energy $\Delta E^{Ln,Ln}$ between two occupied adjacent sites, such linear receptors can be intentionally half-filled with lanthanide cations in order to obtain either metal ion clustering ($\Delta E^{Ln,Ln} < 0$, Figure 2a), a statistical distribution ($\Delta E^{Ln,Ln} \approx 0$, Figure 2b), or metal ion alternation ($\Delta E^{Ln,Ln} > 0$, Figure 2c) in the binding sites.[5] Interestingly, similar behavior is predicted for the saturation of these polymers with two different competitive lanthanide metals, Ln1(50%) and Ln2(50%), if $\Delta E^{Ln,Ln}$ is replaced with the effective pair interaction energy $\Delta E_{eff} = \Delta E^{Ln1,Ln1} + \Delta E^{Ln2,Ln2} - 2\Delta E^{Ln1,Ln2}$.[5] Such unprecedented lanthanide discrimination offers great potential for the design of functional optoelectronic devices that require specific sequences of different metals, for instance in the field of optical downconversion,[6] upconversion,[7] dual analytic probes,[8] and four-level lasers.[9] However, the manipulation of $\Delta E^{Ln,Ln}$ in solution is challenging because the net interaction energy arises from a delicate balance between the intramolecular electrostatic

Received: July 21, 2011
Published: September 01, 2011

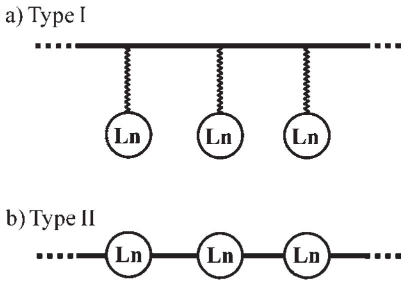

Figure 1. Two different strategies for the introduction of lanthanide-binding sites into organic polymers. The chelating units are (a) connected to the periphery (type I)[3f] or (b) incorporated within the polymer backbone (type II).[4]

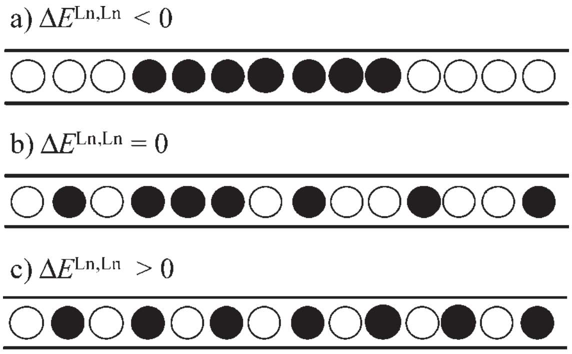

Figure 2. Representation of microstates of half-occupied polymeric linear receptors displaying (a) attractive, (b) negligible, and (c) repulsive nearest-neighbor pair interaction energies.[5]

repulsions of the metal ions and the opposing stabilizing solvation energies; in addition, both of these contributions are highly sensitive to geometrical parameters.[6]

The state-of-the-art for rational control over $\Delta E^{\mathrm{Ln,Ln}}$ is only compatible with the production of rigid linear receptors that possess regularly spaced binding sites, as schematically depicted in Figure 2.[10] Quantification of the geometrical arrangement and thermodynamic parameters of the final metal-loaded polymers would greatly benefit from the use of metal cations that can also function as efficient luminescent reporters.[11] Thus, semirigid polyaromatic tridentate binding units coded for luminescent cations and separated by rigid aromatic spacers are a promising tool for addressing this challenge. This conclusion was already reached by Holliday and co-workers, who took advantage of the electropolymerization of thienyl spacers in **L1** followed by reaction with luminescent Eu(β-diketonate)$_3$,[4a] and by Bai and co-workers, who used Sonogashira coupling reactions to connect tridentate binding units with diacetylene-phenyl spacers in **L2** (Scheme 1). Inspired by these pioneering efforts, we used a Suzuki–Miyaura protocol for coupling two tridentate 2,6-bis(benzimidazol-2-yl)pyridine binding units at the 1,4 positions of the rigid phenyl spacer in **L3**.[12] Because of the restricted number of torsional degrees of freedom imposed by the polyaromatic scaffold ($n = 6$ interannular free rotations, Scheme 1), reaction of **L3** with trivalent lanthanides in acetonitrile shows the formation of the target linear complex $[\mathrm{Ln_2}(\mathbf{L3})]^{6+}$, and a side product of $[\mathrm{Ln_2}(\mathbf{L3})_2]^{6+}$, instead of the usual saturated polycyclic triple-stranded helicates.[13] Pushing this advantage further, we replaced the original $\mathrm{Ln(O_3SCF_3)_3}$ salts with poorly dissociable Ln(hfac)$_3$ metallic units (hfac$^-$ is the didentate hexafluoroacetylacetonate anion)[1] to ensure the formation of the saturated single-stranded complex $[\mathrm{Ln_2}(\mathbf{L3})(\mathrm{hfac})_6]$ as the only stable product of the assembly process. Concomitantly, we exploited this synthetic effort for the development of a simple and general tool for deciphering ligand-centered sensitization in luminescent lanthanide-containing polyaromatic complexes[14] and for the optimization of luminescence efficiency in $[\mathrm{Eu_2}(\mathbf{L}\boldsymbol{k})(\mathrm{hfac})_6]$ ($k = 3$–5) via specific substitutions of the central phenyl spacers with neutral (X = H, **L3**), electron-withdrawing (X = F, **L4**), or electron-donating (X = OCH$_3$, **L5**) groups.

Scheme 1. Chemical Structures of Ligands L1–L7

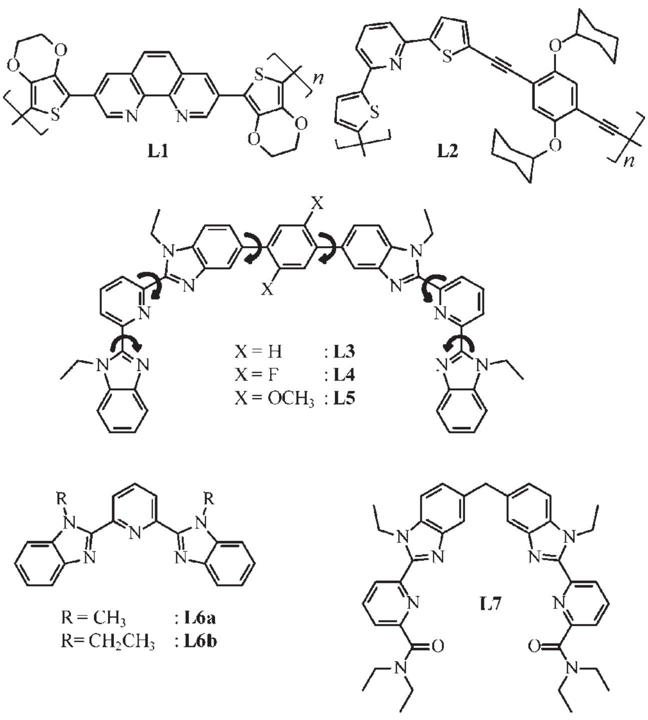

RESULTS AND DISCUSSION

Theoretical Justifications for the Design of Ligands L3–L5. Beyond empirical solubility considerations, the benefit of a substituted phenyl spacer in the ligands **L3**–**L5** strongly depends on the substituent's influence on the photophysics of the final complexes $[\mathrm{Ln_2}(\mathbf{L}\boldsymbol{k})(\mathrm{hfac})_6]$. Since the discovery of the concept of indirect ligand-centered sensitization of lanthanide cations, i.e., the antenna effect, by Weissman in 1942,[15] pertinent energy migration mechanisms have been described and detailed in many reports.[14,16,17] For Eu(III), the accepted model relies on resonant or phonon-assisted feeding of metal-centered excited states from ligand-centered excited $^1\pi\pi^*$ or $^3\pi\pi^*$ levels when their characteristic lifetimes are long enough to significantly contribute to the global energy transfer.[17] Given the experimental ligand-centered fluorescence lifetimes of only 30–70 ps that are measured for the $[\mathrm{Gd_2}(\mathbf{L}\boldsymbol{k})(\mathrm{hfac})_6]$ ($\mathbf{L}\boldsymbol{k}$ = **L3**–**L5**, Table 2, *vide infra*) complexes, it appears likely that the energy migration processes in $[\mathrm{Eu_2}(\mathbf{L}\boldsymbol{k})(\mathrm{hfac})_6]$ can be satisfyingly modeled with the exclusive contribution of the triplet state as shown in Figure 3.[14,16] With this hypothesis in mind, it is worth noting

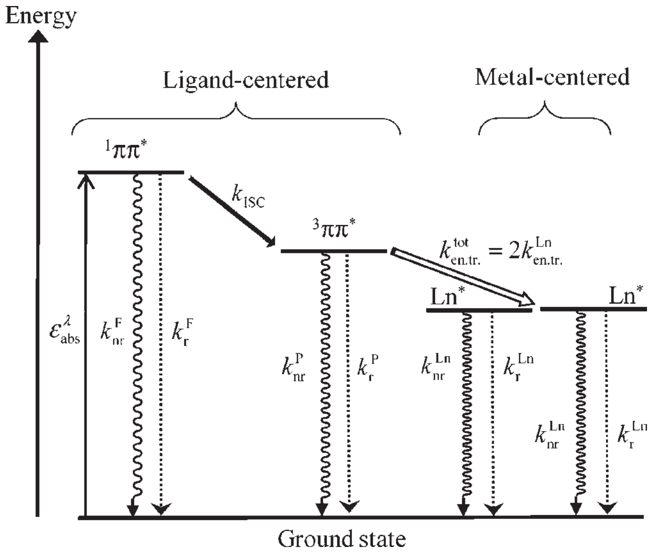

Figure 3. Simplified Jablonski diagram for $[Ln_2(\mathbf{L}\mathit{k})(hfac)_6]$ (k = 3−5), showing the ligand-centered triplet-mediated sensitization mechanism of the two trivalent lanthanides.[20] k^F_r and k^F_{nr}, radiative and nonradiative fluorescence rate constants; k^P_r and k^P_{nr}, radiative and nonradiative phosphorescence rate constants; k^{Ln}_r and k^{Ln}_{nr}, radiative and nonradiative metal-centered rate constants; k_{ISC}, intersystem crossing rate constant; and $k^{tot}_{en.tr.}$, global ligand-to-metal energy-transfer rate constant.[19]

that the rate eqs 1−5 describe the efficiency of the indirect ligand-centered sensitization of Ln(III). In these equations, $\Phi^{Ln}_{Ln}(F)$ and $\Phi^{Ln}_{Ln}(P)$ are the intrinsic ligand-centered quantum yields of fluorescence and phosphorescence, respectively; Φ^L_L is the intrinsic metal-centered quantum yield of luminescence;[18] η_{ISC} and $\eta^{L\rightarrow Ln}_{en.tr.}(P)$ are the efficiencies of intersystem crossing and ligand-to-metal energy-transfer processes, respectively;[19] and $\tau_L(F)$ and $\tau_L(P)$ are the characteristic excited-state lifetimes of ligand-centered fluorescence and phosphorescence, respectively. τ_{Ln} is the excited-state lifetime of the metal-centered luminescence. The definition of each individual rate constant is given in the caption of Figure 3.

$$\Phi^L_L(F) = \frac{k^F_r}{k^F_r + k^F_{nr} + k_{ISC}} = k^F_r \tau_L(F) \quad (1)$$

$$\Phi^L_L(P) = \frac{k^P_r}{k^P_r + k^P_{nr} + k^{tot}_{EnT}} = k^P_r \tau_L(P) \quad (2)$$

$$\Phi^{Ln}_{Ln} = \frac{k^{Ln}_r}{k^{Ln}_r + k^{Ln}_{nr}} = k^{Ln}_r \tau_{Ln} \quad (3)$$

$$\eta_{ISC} = \frac{k_{ISC}}{k^F_r + k^F_{nr} + k_{ISC}} = k_{ISC}\tau_L(F) \quad (4)$$

$$\eta^{L\rightarrow Ln}_{en.tr.}(P) = \frac{k^{tot}_{en.tr.}}{k^P_r + k^P_{nr} + k^{tot}_{en.tr.}} = k^{tot}_{en.tr.}\tau_L(P) \quad (5)$$

The overall luminescence intensity I^L_{Ln} (eq 6),[14a,21] expressed in $M^{-1}\cdot cm^{-1}$, combines the contribution of the light-harvesting step (measured by the molar absorption coefficients $\varepsilon^{\lambda}_{abs}$ of the ligand-centered $^1\pi\pi\rightarrow{}^1\pi\pi^*$ transition) with that of the global quantum yield Φ^L_{Ln} characterizing the complete energy migration scheme (eq 7).[14]

$$I^L_{Ln} = \varepsilon^{\lambda}_{abs}\Phi^L_{Ln} \quad (6)$$

$$\Phi^L_{Ln} = \eta_{ISC}\eta^{L\rightarrow Ln}_{en.tr.}(P)\Phi^{Ln}_{Ln} \quad (7)$$

The intrinsic lanthanide quantum yield Φ^{Ln}_{Ln} (eq 3) has been the subject of considerable investigations,[18a,22] and its rationalization in coordination complexes relies on the Judd−Ofelt theory, which considers odd-rank crystal-field contributions as the origin of the non-negligible radiative rate k^{Ln}_r,[23] while vibrationally coupled deactivation pathways control k^{Ln}_{nr}.[24] These parameters are not particularly sensitive to substituents on the phenyl spacer in $[Ln_2(\mathbf{L}\mathit{k})(hfac)_6]$ (k = 3−5), and thus Φ^{Ln}_{Ln} is not expected to vary significantly in these complexes. The next important contribution to the overall emission yield is the efficiency of the ligand-to-metal energy transfer $\eta^{L\rightarrow Ln}_{en.tr.}(P)$ (eq 5), which has also undergone intense investigations in recent decades.[11,14,16,24,25] Assuming the exclusive contribution of the triplet mechanism for Eu sensitization, a good match between the energy of the donor ligand-centered $^3\pi\pi^*$ excited state and the accepting Eu(III) excited levels is a prerequisite for optimizing $\eta^{L\rightarrow Ln}_{en.tr.}(P)$.[26] Because the energy of the ligand-centered triplet state may be influenced by the substituents on the central phenyl ring in **L3**−**L5**, this factor should be considered in the ligand design. Surprisingly, the parameters influencing η_{ISC} (eq 4) in lanthanide complexes have been rarely studied in detail or systematically optimized, except for (i) the elucidation of the origin of the favorable heavy-atom and paramagnetic effects produced by the coordination of open-shell Ln(III) to aromatic ligands,[27] and (ii) the intrinsic advantage of using fused polyaromatic scaffolds as antennae for sensitizing Eu and Tb.[28] Equation 4 suggests that η_{ISC} may be further optimized when the sum of the rate constants $k^F_r + k^F_{nr}$ is negligible with respect to k_{ISC} (i.e., $k^F_r + k^F_{nr} \ll k_{ISC}$). Following Yamaguchi and co-workers, the k^F_r and k^F_{nr} rate constants in polyaromatic systems correlate with the so-called π-conjugation length A_π (no unit), which is proportional to the charge displacement that is induced in the excited state by the $^1\pi\pi\rightarrow{}^1\pi\pi^*$ transition of the organic scaffold.[29]

$$k^F_r = k^F_{nr}\, e^{A_\pi} \quad (8)$$

We immediately deduce from eq 8 that $k^F_r + k^F_{nr} = k^F_{nr}(1 + e^{A_\pi})$ has its minimum value when both k^F_{nr} and A_π are minimized. A significant tuning of k^F_{nr} is not expected for minor changes in the substitution of the central phenyl ring in **L3**−**L5**. However, A_π could be seriously affected if the relevant low-energy $^1\pi\pi\rightarrow{}^1\pi\pi^*$ transition possesses charge-transfer character involving the phenyl spacer. In order to address this specific point, DFT calculations were performed on the noncomplexed ligand strands. First, we note that the computationally optimized gas-phase centrosymmetric structures are very similar for the three ligands **L3**−**L5**, except for a small stepwise increase of the interannular torsion angles between the central 1,4-disubstituted phenyl spacer and the adjacent 5-benzimidazole rings ($\alpha(\mathbf{L3}) = 35.5°$[30] $< \alpha(\mathbf{L4}) = 38.9° < \alpha(\mathbf{L5}) = 45.0°$; see Figure 4 and Figure S1 in the Supporting Information). Second, the calculated frontier orbitals show the HOMOs to be located on the central bis(benzimidazole)phenyl spacer and the LUMOs to lie on the terminal benzimidazole-pyridine rings of each binding unit (Figure 4).

Thus, substitution of the central phenyl rings mainly affects the energy of the HOMO, while that of the LUMO is only marginally

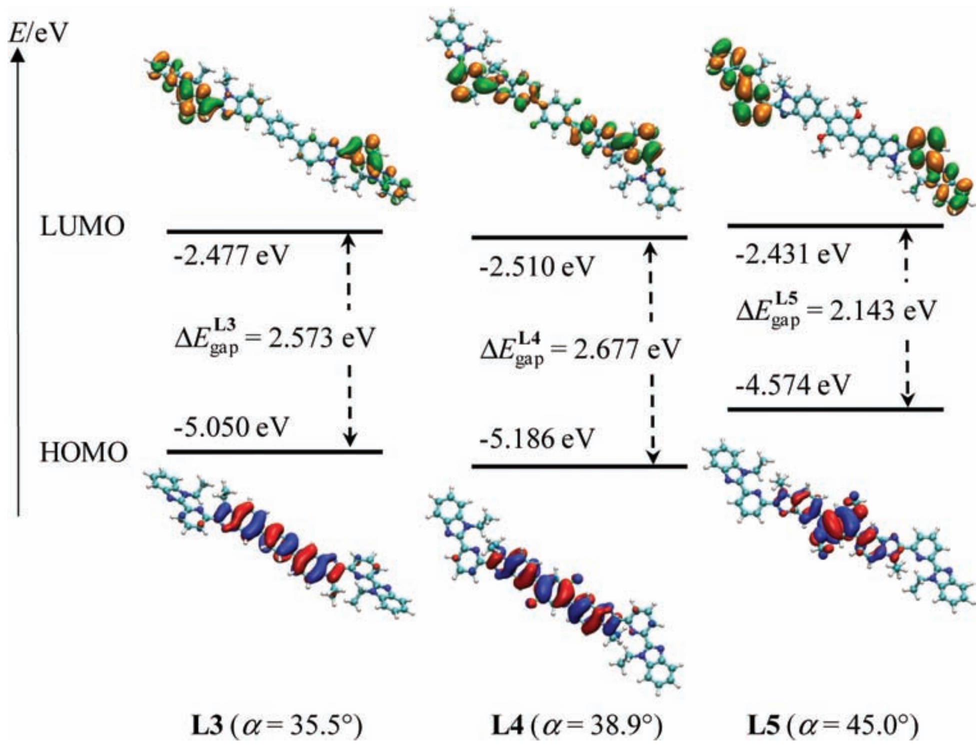

Figure 4. Frontier orbitals, computed by DFT, for **L3**−**L5** in their optimized gas-phase geometries (1 eV = 8065.5 cm^{-1}).

Scheme 2. Synthesis Scheme and Numbering Scheme for ^{1}H NMR of Ligands L3−L5

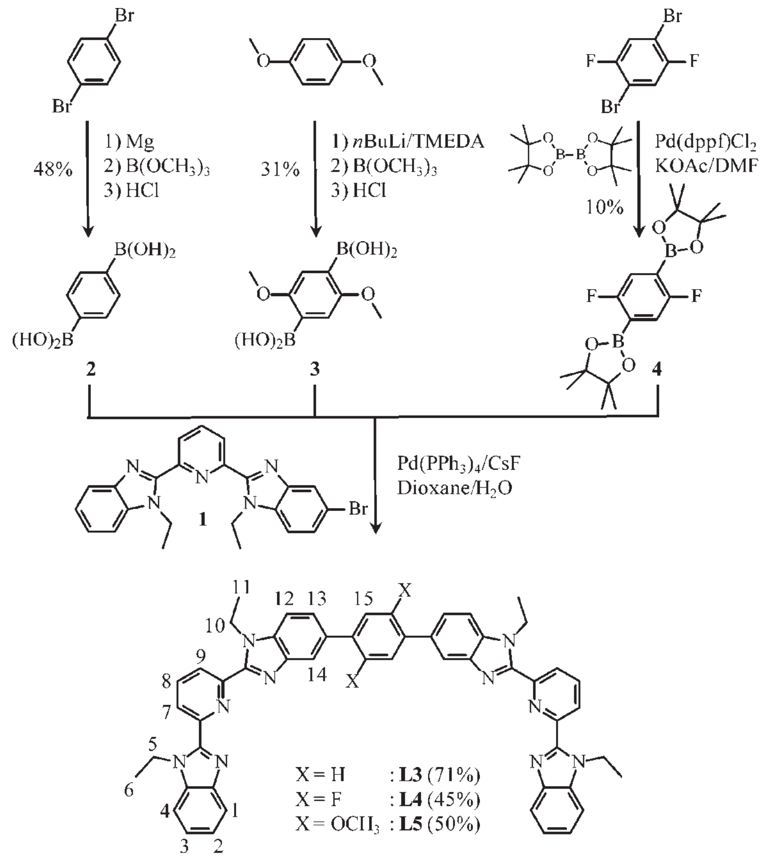

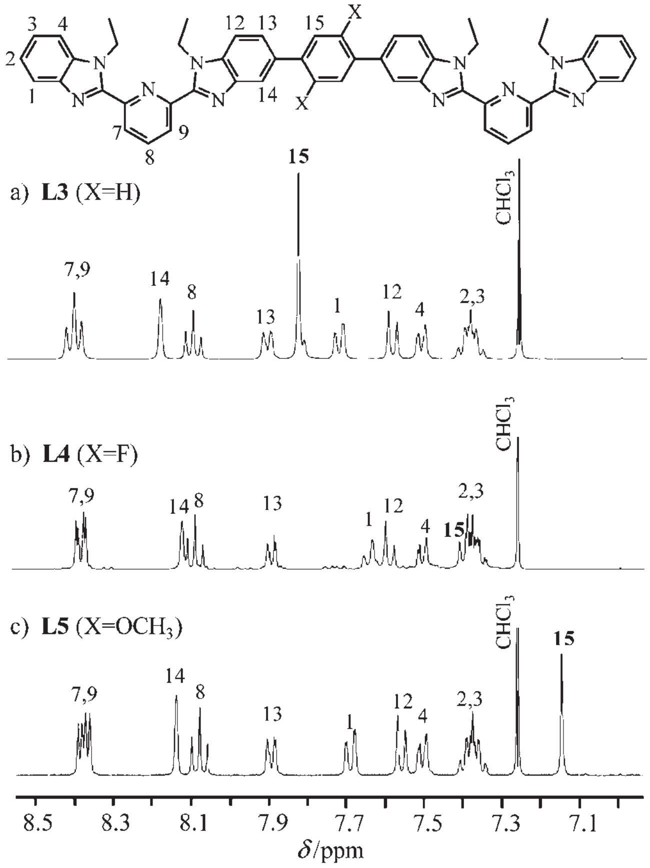

Figure 5. Aromatic parts of the ^{1}H spectra of **L3**−**L5** in CDCl$_3$ at 293 K.

affected. Consequently, the HOMO−LUMO energy gap increases as the electron-withdrawing capacity of the substituent increases; i.e., $\Delta E_{\mathrm{gap}}^{\mathbf{L5}}$ (X = OCH$_3$) < $\Delta E_{\mathrm{gap}}^{\mathbf{L3}}$ (X = H) < $\Delta E_{\mathrm{gap}}^{\mathbf{L4}}$ (X = F). Taking the trend in the HOMO→LUMO transition as a guide for how the π-conjugation length changes, we conclude that the variable charge-transfer character of this transition in **L3**−**L5** may significantly affect this parameter. Thus, **L3**−**L5** are good candidates for simultaneously optimizing solubilities and ligand-centered photophysical properties, while minimizing structural variations and synthetic efforts and preserving metal-centered photophysical properties.

Synthesis, Structures, and Photophysical Properties of the Bis-tridentate Ligands L3−**L5.** The formation of two C$_{\mathrm{arom}}$−C$_{\mathrm{arom}}$ bonds is achieved via a Miyaura−Suzuki strategy[12] using the mono-brominated compound **1** (Scheme S1, appendix 4 in the Supporting Information). Reactions of the bis-boronic acids **2** and **3**[31] or the bis-boronic ester **4**[32] (1 equiv) with **1** (2 equiv) using standard Pd(0)-catalyzed conditions[12] provide **L3**−**L5** in acceptable yields (Scheme 2). Because of the existence of an average twofold symmetry axis in solution (C_2 or $S_2 = C_i$, Figure 5 and Table S1), the ^{1}H NMR spectrum of each ligand exhibits 15 signals (Figure S2); this pattern disqualifies arrangement **I** among the four static limiting structures shown in Scheme 3. The systematic detection of enantiotopic pairs for the methylene protons H5 and H10 (numbering in Scheme 2 and Figure S2) discards structures **III** and **IV** because of the lack of the required additional symmetry plane for X = F, OCH$_3$. Ligands **L3**−**L5** thus adopt the average planar S-shaped arrangement **II** in chloroform, in agreement with the optimized DFT organization computed in the gas phase.

Scheme 3. Possible Static Geometries for the Central Bis(benzimidazole)phenyl Spacer for Ligands L3−**L5 in Solution**[a]

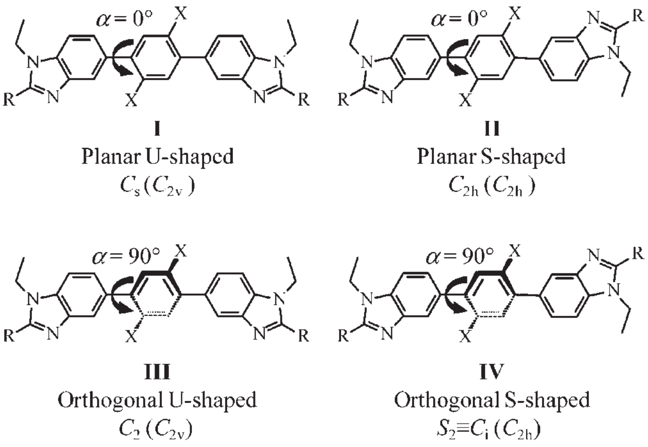

[a] Point groups are given for X ≠ H, while the related point groups for X = H are given in parentheses.

Interestingly, the singlet observed for H15 is the only ^{1}H NMR signal that is sensitive to the nature of the substituent for **L3**−**L5** (Figure 5).[33] This observation implies a limited conjugation of the central aromatic core in solution, which can be tentatively assigned to fast rotations and/or oscillations of the central substituted phenyl spacers on the NMR time scale at room temperature, an interpretation in complete agreement with the small activation energies reported for interaromatic rotations occurring in closely related diethyl-substituted terphenyl.[34]

The electronic absorption spectra recorded in dichloromethane are similar for **L3**−**L5** and show a broad and intense spin-allowed low-energy $\pi\rightarrow\pi^*$ transition centered around 30 000 cm^{-1} (Table 1 and Figure S3). The decreasing energy order **L4** > **L3** > **L5** found for the latter transition is also apparent in their associated emission spectra, in which the emission maxima follow the trend 25 400 (**L4**) > 23 900 (**L3**) > 22270 cm^{-1} (**L5**). These observations are in qualitative agreement with DFT calculations (Figure 6a and Table 1). The same trend is retained in frozen solution at 77 K (Figure S4); however, the emission band envelopes shift slightly because of the thermal redistribution of the vibrational-level populations and the possible blocking of the internal interannular rotations at low temperature (Figure S5).[34] Surprisingly, the position of the weak, but reliable, emission of the ligand-centered triplet states is not sensitive to the substitution of the phenyl spacer, and an average value of 20 200 cm^{-1} can be assigned to all **L*k***($^3\pi\pi^*$) excited states at 77 K (Table 1, Figure 6b).

The absolute quantum yields of fluorescence of **L3**−**L5** in solution are considerable ($0.4 \leq \Phi_{\mathrm{L}}^{\mathrm{L}}(\mathrm{F}) \leq 0.8$; see Table 2, column 5), and their combination with the **L*k***($^1\pi\pi^*$) fluorescence lifetimes ($\tau_{\mathrm{L}}(\mathrm{F})$, Table 2, column 6) via eq 1 gives radiative fluorescence rate constants $k_{\mathrm{r}}^{\mathrm{F}}$ that follow a trend consistent with the Einstein equation for spontaneous emission (**L4** > **L3** > **L5**; see Table 2, column 7).[35] The sums of the nonradiative rate constants $k_{\mathrm{nr}}^{\mathrm{F}} + k_{\mathrm{ISC}}$ remain similar for the three ligands within experimental errors (Table 2, column 8). Following Yamaguchi and co-workers, who reasonably assumed that $k_{\mathrm{ISC}} \ll k_{\mathrm{nr}}^{\mathrm{F}}$ for free polyaromatic ligands,[29] eq 8 provides π-conjugation lengths of $-0.4 \leq A_\pi \leq 1.4$ for **L3**−**L5** in solution (Table 2, column 12),

Table 1. Ligand-Centered Absorption and Emission Properties of L3−L6 and Their Complexes $[Gd_2(\mathbf{L}k)(hfac)_6]$

compd	T/K	$\lambda_{max,abs}$/cm^{-1} [a] $^1\pi\pi\rightarrow{}^1\pi\pi^*$	$\lambda_{max,flu}$/cm^{-1} $^1\pi\pi^*\rightarrow{}^1\pi\pi$	lifetime/ns $\tau(^1\pi\pi^*)$	$\lambda_{max,phos}$/cm^{-1} $^3\pi\pi^*$	lifetime/ms $\tau(^3\pi\pi^*)$
			Solution (CH_2Cl_2)			
L3	293	34 250 (57 000)	23 900	2.04(7)		
	77	29 850 (69 500)	24 650		20 200	–[b]
L4	293	37 480 (43 400)	25 400	1.374(4)		
	77	29 860 (73 300)	25 500		20 240	–[b]
L5	293	36 850 (50 320)	22 200	2.37(18)		
	77	29 590 (73 300)	24 300		20 200	–[b]
L6a[c]	293	41 360 (16 000)	27 100	1.9(1)		
	77	30 980 (35 000)	26 400		22 000	–[b]
			Solid State			
L3	293	29 850	23 350	0.149(12)		
	77		23 310		18 720	–[b]
L4	293	29 660	24 180	0.160(3)		
	77		25 250		19 480	–[b]
L5	293	29 590	24 540	0.221(7)		
	77		24 600		19 470	–[b]
$[Gd_2(\mathbf{L3})(hfac)_6]$	293	28 650	22 620	0.060(2)	19 070	0.123(7)
	77		22 600		19 070	0.69(5)
$[Gd_2(\mathbf{L4})(hfac)_6]$	293	28 650	23 820	0.066(14)	19 470	0.16(2)
	77		22 700		19 470	0.67(5)
$[Gd_2(\mathbf{L5})(hfac)_6]$	293	28 730	23 780	0.028(16)	19 100	0.141(6)
	77		22 100		19 100	0.69(5)

[a] The molar absorption coefficients ε (in M^{-1} cm^{-1}) are given in parentheses. [b] The intensity is too weak to obtain reliable lifetime measurements. [c] Taken from ref 21b and recorded in CH_3CN.

which make these centrosymmetrical bis-tridentate polyaromatic ligands comparable to triphenylene (A_π = −0.04) and tetraphenylene (A_π = 1.82).[29] Comparison of the photophysical and spectral properties of **L3**−**L5** with those of the precursor ligand **L6a** shows that the connection of two tridentate bis(benzimidazol-2-yl)pyridine units via substituted aromatic phenyl spacers in **L3**−**L5** has two major consequences. First, both electronic absorption ($^1\pi\pi\rightarrow{}^1\pi\pi^*$, Figure S3) and emission ($^1\pi\pi^*\rightarrow{}^1\pi\pi$ and $^3\pi\pi^*\rightarrow{}^1\pi\pi$) transitions of **L3**−**L5** are red-shifted by 1800−4800 cm^{-1} (Table 1). Second, novel nonradiative deactivation pathways are present for **L3**−**L5**, and they limit the fluorescence quantum yields (Table 2). Note that, upon crystallization, the fluorescence quantum yields $\Phi_L^L(F)$ and fluorescence lifetimes $\tau_L(F)$ concomitantly decrease by more than 1 order of magnitude (Table 2, columns 5 and 6), while the calculated radiative rate constant (eq 1) remains constant (Table 2, column 7). This observation indicates that the nonradiative rate constants are magnified by the additional intermolecular interactions in the solid state (Table 2, column 8).

Synthesis, Structures, and Stabilities of the Dinuclear Complexes $[Ln_2(\mathbf{L}k)(hfac)_6]$ (Ln = Gd, Eu, Y; L*k* = L3−L5). Reaction of **L*k*** (1 equiv) with $[Ln(hfac)_3diglyme]$ (2.0 equiv, Ln = Gd, Eu, Yb, Y)[38] in chloroform yields 50−90% of $[Ln_2(\mathbf{L}k)(hfac)_6]$ as microcrystalline precipitates (Table S2). Subsequent recrystallizations by slow diffusion of diethyl ether into saturated acetonitrile/chloroform solutions of the complexes provide X-ray-quality prisms for $[Yb_2(\mathbf{L3})(hfac)_6]$ (**1**), $[Y_2(\mathbf{L3})(hfac)_6]$ (**2**), $[Yb_2(\mathbf{L4})(hfac)_6]$ (**3**), and $[Eu_2(\mathbf{L5})(hfac)_6]$ (**4**) (Table S3). The crystal structures can be described as packed neutral dinuclear complexes held together by networks of intermolecular π-stacking interactions (Figures S6−S8). As expected, the size of the lanthanide cation does not greatly affect the crystal organization, and $[Yb_2(\mathbf{L3})(hfac)_6]$ (**1**) is thus isostructural with $[Y_2(\mathbf{L3})(hfac)_6]$ (**2**, Table S3 and Figure S9). Only the former complex will be considered for further comparisons with **3** and **4**. Each dinuclear complex possesses a crystallographic symmetry element passing through the substituted phenyl ring, leading to a twofold U-shaped arrangement of the ligand strand in $[Yb_2(\mathbf{L3})(hfac)_6]$ (Yb···Yb = 12.624(2) Å, Figure 7a) and centrosymmetrical S-shaped geometries in $[Yb_2(\mathbf{L4})(hfac)_6]$ (Yb···Yb = 14.77(1) Å, Figure 7b) and $[Eu_2(\mathbf{L5})(hfac)_6]$ (Eu···Eu = 14.928(3) Å, Figure 7c).

Each trivalent lanthanide cation in $[Ln_2(\mathbf{L}\boldsymbol{k})(hfac)_6]$ is nine-coordinated by the three nitrogen donor atoms of the 2,6-bis(benzimidazol-2-yl)pyridine moiety and the six oxygen atoms of three didentate $hfac^-$ anions, forming distorted polyhedra (Figure 7). The Ln−O[39] and Ln−N[40] distances are typical of those found in other complexes (Table 3 and Tables S4−S11). Close scrutiny of the bond valences $\nu_{Ln,N}$ and $\nu_{Ln,O}$ (Tables S12−S14)[41] shows that the replacement of the nitrate groups found in the model complex $[Eu(\mathbf{L6})(NO_3)_3]$ ($\nu_{Eu,N(bzim)}$ = 0.39, $\nu_{Eu,N(py)}$ = 0.29, and $\nu_{Eu,O\text{-}nitrate}$ = 0.28)[40] with hexafluoroacetylacetonate in $[Ln_2(\mathbf{L}\boldsymbol{k})(hfac)_6]$ is accompanied by a significant reduction of $\nu_{Ln,N(bzim)}$ and $\nu_{Ln,N(py)}$ that is compensated by a parallel increase of $\nu_{Ln,O\text{-anion}}$ (Table 3). We deduce that the $hfac^-$ counter-anions exhibit stronger interactions with Ln(III) than does NO_3^-, and the resulting decrease of the metal's effective positive charge reduces the affinity of $Ln(hfac)_3$ for the tridentate site in $[Ln_2(\mathbf{L}\boldsymbol{k})(hfac)_6]$ (see Table 3).

This trend is further substantiated by the observed decrease, 2−3 orders of magnitude, in the thermodynamic formation constants that are measured in acetonitrile when NO_3^- counter-anions (eq 9; $\log(\beta_{2,1}^{Y,\mathbf{L7}})$ = 10.12(9), see Scheme 1 for the structure of **L7**)[42] are replaced with $hfac^-$ counter-anions (eq 10; $\log(\beta_{2,1}^{Y,\mathbf{L3}})$ = 7.3(2), $\log(\beta_{2,1}^{Y,\mathbf{L4}})$ = 6.6(3), $\log(\beta_{2,1}^{Y,\mathbf{L5}})$ = 8.4(5), see appendix 1 in the Supporting Information for details).

$$2Y(NO_3)_3 + \mathbf{L7} \rightleftharpoons [Y_2(\mathbf{L7})(NO_3)_6] \quad \beta_{2,1}^{Y,\mathbf{L7}} \tag{9}$$

$$2Y(hfac)_3 + \mathbf{L}\boldsymbol{k} \rightleftharpoons [Y_2(\mathbf{L}\boldsymbol{k})(hfac)_6] \quad \beta_{2,1}^{Y,\mathbf{L}\boldsymbol{k}} \tag{10}$$

Finally, it is worth noting that the stepwise insertion of bulkier substituents onto the central phenyl ring (X = H (**L3**) < X = F (**L4**) ≈ X = OCH_3 (**L5**)) substantially increases the interannular phenyl−benzimidazole interplanar angles from α = 25.26(4)° in $[Yb_2(\mathbf{L3})(hfac)_6]$ to α = 54.1(1)° in $[Yb_2(\mathbf{L4})(hfac)_6]$ and to 45.34(4)° in $[Eu_2(\mathbf{L5})(hfac)_6]$ (Tables S5, S9, and S11). This change in twist angle should affect the HOMO−LUMO gap in the various complexes, but it is not expected to change the trend in the HOMO−LUMO gap through the series, i.e., $\Delta E_{gap}^{\mathbf{L5}}$ (X = OCH_3) < $\Delta E_{gap}^{\mathbf{L3}}$ (X = H) < $\Delta E_{gap}^{\mathbf{L4}}$ (X = F) (Figure S5).

Photophysical Properties of the Dinuclear Complexes $[Ln_2(\mathbf{L}\boldsymbol{k})(hfac)_6]$ (Ln = Gd, Eu; L*k* = L3−L5). Taking $\log(\beta_{2,1}^{Y,\mathbf{L}\boldsymbol{k}})$ estimated in acetonitrile for eq 10, we calculate that millimolar concentrations are required to ensure that more than 80% of $[Y_2(\mathbf{L}\boldsymbol{k})(hfac)_6]$ is formed in solution (Table S15). Because of the sub-millimolar solubilities of these complexes (Figure S10),

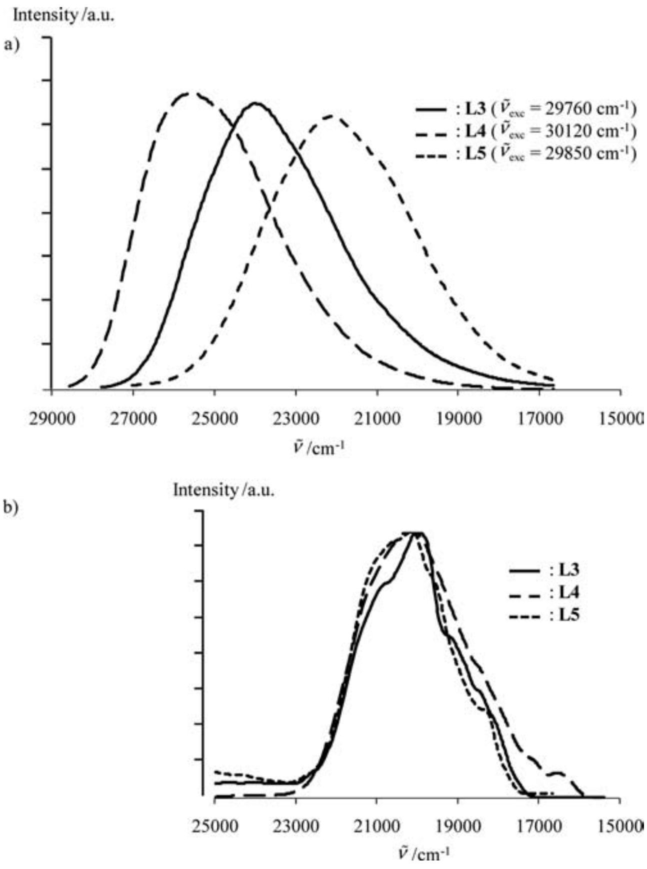

Figure 6. (a) Fluorescence (293 K) and (b) phosphorescence (delay time after excitation flash 0.1 ms, 77 K) emission spectra for **L3**−**L5** in solution (10^{-4} M in CH_2Cl_2).

Table 2. Fluorescence Quantum Yields ($\Phi_L^L(F)$) and Lifetimes ($\tau_L(F)$), Computed Rate Constants (k_r^F, k_{nr}^F, and k_{ISC}) and π-Conjugation Lengths (A_π) for L3−L6 and Their Complexes $[Gd_2(\mathbf{L}\boldsymbol{k})(hfac)_6]$ at 293 K

compd	concn/M	$\bar{\nu}_{exc}/cm^{-1}$	$\varepsilon(\bar{\nu}_{exc})/M^{-1}\,cm^{-1}$	$\Phi_L^L(F)$	$\tau_L(F)/ns$	k_r^F/ns^{-1}	$k_{nr}^F + k_{ISC}/ns^{-1}$	$k_{ISC}{}^a/ns^{-1}$	$\eta_{ISC}{}^a$	$k_{nr}^F{}^b/ns^{-1}$	A_π
					Solution (CH_2Cl_2)						
QSO_4[c]	6.42×10^{-6}	27 780	8100	0.546							0.18
L3	10^{-5}	27 780	4000	0.80(8)	2.04(7)	0.39(4)	0.10(7)				1.39(6)
L4	10^{-5}	27 780	4300	0.74(8)	1.374(4)	0.54(6)	0.17(2)				1.05(7)
L5	10^{-5}	27 780	3300	0.40(5)	2.37(18)	0.19(10)	0.25(4)				−0.41(8)
L6a[d]	9.86×10^{-5}	28 820	5130	1.00(7)	1.9(1)	0.53(5)	0.00(6)				
					Solid State						
L3		29 550		0.045(2)	0.149(12)	0.30(3)	6.41(4)				−3.05(3)
L4		29 550		0.049(2)	0.160(3)	0.31(1)	5.94(2)				−2.97(3)
L5		29 550		0.023(1)	0.221(7)	0.104(6)	4.421(9)				−3.75(3)
$[Gd_2(\mathbf{L3})(hfac)_6]$		29 850		0.00316(7)	0.060(2)	0.053(2)	16.6(7)	10.0(6)	0.60(3)	6.7(8)	−4.84(5)
$[Gd_2(\mathbf{L4})(hfac)_6]$		29 850		0.0035(5)	0.066(14)	0.05(1)	15(4)	9(2)	0.6(1)	6(4)	−4.8(3)
$[Gd_2(\mathbf{L5})(hfac)_6]$		29 850		0.0027(10)	0.028(16)	0.09(7)	36(24)	31(18)	0.9(5)	4(27)	−3.8(2.7)

[a] k_{ISC} is estimated for $[Gd_2(\mathbf{L}\boldsymbol{k})(hfac)_6]$ with eq 11 and η_{ISC} with eq 4 (see text). [b] $k_{nr}^F = (1/\tau_L(F)) - k_{ISC} - k_r^F$. [c] Quinine sulfate in 0.05 M H_2SO_4.[37] [d] Taken from ref 21b and recorded in CH_3CN.

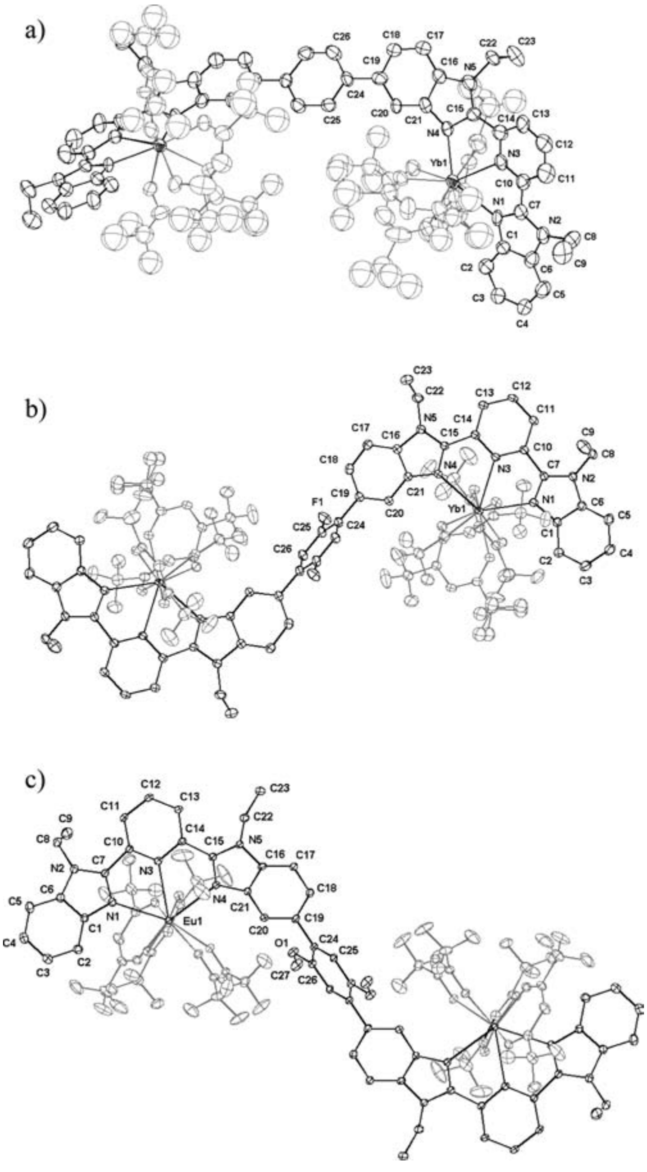

Figure 7. ORTEP views of the molecular structures with the numbering schemes for (a) $[Yb_2(\mathbf{L3})(hfac)_6]$, (b) $[Yb_2(\mathbf{L4})(hfac)_6]$, and (c) $[Eu_2(\mathbf{L5})(hfac)_6]$ in the crystal structures of **1**, **3**, and **4**. Thermal ellipsoids are represented at the 30% probability level, and hydrogen atoms are omitted for clarity.

Table 3. **Ln···Ln, Ln−N, and Ln−O Distances (Å), Bond Valences ($\nu_{Ln,j}$),[a] and Bond Valence Sums (V_{Ln})[b] in the Crystal Structures of $[Yb_2(L3)(hfac)_6]$ (1), $[Yb_2(L4)(hfac)_6]$ (3), and $[Eu_2(L5)(hfac)_6]$ (4)**

	$[Yb_2(\mathbf{L3})(hfac)_6]$	$[Yb_2(\mathbf{L4})(hfac)_6]$	$[Eu_2(\mathbf{L5})(hfac)_6]$
$Ln{-}N_{bzim}{}^{c}$/Å	2.443(4)	2.476(4)	2.581(1)
$Ln{-}N_{py}$/Å	2.519	2.526	2.61
$Ln{-}O^{d}$/Å	2.38(8)	2.36(7)	2.43(2)
Ln···Ln/Å	12.624	14.77	14.928
$\nu_{Ln,N(bzim)}{}^{c}$	0.359(4)	0.328(4)	0.322(1)
$\nu_{Ln,N(py)}$	0.292	0.287	0.297
$\nu_{Ln,O}{}^{d}$	0.33(6)	0.34(6)	0.35(2)
V_{Ln}	2.964	2.980	3.039

[a] $\nu_{Ln,j} = e[(R_{Ln,j} - d_{Ln,j})/b]$, where $d_{Ln,j}$ is the Ln−donor atom j distance. The valence bond parameters $R_{Ln,N}$ and $R_{Ln,O}$ are taken from refs 41e and 41f, and b = 0.37 Å. [b] $V_{Ln} = \Sigma_j \nu_{Ln,j}$.[41] [c,d] Each value is the average of two[c] or six[d] bond distances, and the numbers in parentheses correspond to the standard deviations affecting the average values (the original uncertainties affecting each bond length are given in Tables S4, S8, and S10; bzim = benzimidazole and py = pyridine).

the photophysical investigations were strictly limited to solid-state samples, where quantitative complexation has been firmly established by X-ray diffraction studies. According to standard protocols,[2,26] the ligand-centered photophysical properties were investigated in the gadolinium complexes $[Gd_2(\mathbf{L}\boldsymbol{k})(hfac)_6]$ because paramagnetic Gd(III) induces some mixing of ligand and metal wave functions, similar to that expected upon complexation of luminescent Eu(III) (heavy-atom effect and paramagnetic coupling).[27] Moreover, Gd(III) does not possess low-lying metal-centered excited-state levels that could participate in energy transfer from either $\mathbf{L}\boldsymbol{k}(^1\pi\pi^*)$ or $\mathbf{L}\boldsymbol{k}(^3\pi\pi^*)$.[43]

The UV−vis absorption spectrum of $[Gd_2(\mathbf{L3})(hfac)_6]$, corrected for partial dissociation, appears to combine the characteristics of the $[Gd(hfac)_3]$ unit at high energy (a main band is present at 33060 cm^{-1}) with those of the **L3**-coordinated Gd(III) at low energy; the **L3**-centered $\pi \rightarrow \pi^*$ transition is split by a Davydov exciton coupling, giving bands with apparent maxima at 30 000 and 27 000 cm^{-1} (Figure 8).[44,45]

The **L*k***-centered irradiation of solid-state samples of $[Gd_2(\mathbf{L}\boldsymbol{k})(hfac)_6]$ at $\bar{\nu}_{exc}$ = 28 650 cm^{-1} provides a short-lived fluorescence that is centered near $E(^1\pi\pi^*)$ = 23 000−22 000 cm^{-1}, with a lifetime $\tau_L(F)$ = 30−70 ps at 293 K (see Figure 9a and Table 1) and a weaker, long-lived phosphorescence band located at lower energy ($E(^3\pi\pi^*)$ = 19 500−19 000 cm^{-1}, $\tau_L(P)$ = 123−160 μs at 293 K, Figure 9b and Table 1). Since the excited states centered on the coordinated $hfac^-$ anions are located at energies exceeding 30 000 cm^{-1} (Figure 8),[46] they cannot significantly contribute to the luminescence process in the target complexes $[Gd_2(\mathbf{L}\boldsymbol{k})(hfac)_6]$ for excitation energies below 29 000 cm^{-1}, and the emission characteristics collected for the Gd complexes in Tables 1 and 2 can thus be safely assigned as originating from the coordinated bis-tridentate ligand strands. The predicted and observed decrease of the energy of the $\mathbf{L}\boldsymbol{k}(^1\pi\pi^*)$ excited states along the series **L4** > **L3** > **L5** (Figure 6) is globally retained upon complexation in $[Gd_2(\mathbf{L}\boldsymbol{k})(hfac)_6]$ (Figure 9a), as are the energies characterizing the ligand-centered triplet states (Figure 9b). Compared to the free ligands, the values of the fluorescence quantum yields $\Phi_L^L(F)$ are reduced by an order of magnitude in the associated Gd complexes, while the characteristic $^1\pi\pi^*$ lifetimes only decrease by a factor of 3−5 (Table 2, columns 5 and 6). Consequently, we deduce from eq 1 that the radiative rate constants k_r^F of the ligand-centered $^1\pi\pi^*$ levels are significantly reduced in $[Gd_2(\mathbf{L}\boldsymbol{k})(hfac)_6]$, while that for the overall nonradiative processes, $k_{nr}^F + k_{ISC}$, increases (Table 2, columns 7 and 8).[27] Because $I(^3\pi\pi^*)/I(^1\pi\pi^*) = 2.1 \times 10^{-4}$ for the similar tridentate binding unit in **L6a**,[21] we can reasonably assume that $k_{ISC}(\mathbf{L}\boldsymbol{k}) \ll k_{ISC}([Gd_2(\mathbf{L}\boldsymbol{k})(hfac)_6]$, and k_{ISC}^{Gd} in the Gd complexes can then be roughly estimated with eq 11 (Table 2, column 9).[47] Once k_{ISC}^{Gd} is obtained, then (i) the value of η_{ISC} can be found by using eq 4 (Table 2, column 10), (ii) $k_{nr}^F = (1/\tau_L(F)) - k_{ISC}^{GD} - k_r^F$ is obtained from the definition of the luminescence lifetime (Table 2, column 11), and (iii) A_π is

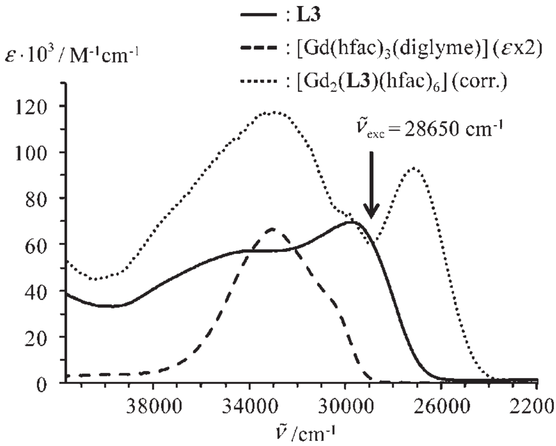

Figure 8. UV−vis absorption spectra for **L3** (CH_2Cl_2, solid line), $[Gd(hfac)_3(diglyme)_2]$ (CH_3CN, dashed line, $\varepsilon \times 2$ for comparison purpose), and $[Gd_2(\mathbf{L3})(hfac)_6]$ (CH_2Cl_2:CH_3CN 1:1, dotted line) recorded at 293 K. The absorption spectrum of the latter ternary complex is corrected for partial decomplexation according to eq 10 with $\log(\beta_{2,1}^{Gd,L3}) \approx 8$ (see appendix 2 in the Supporting Information).

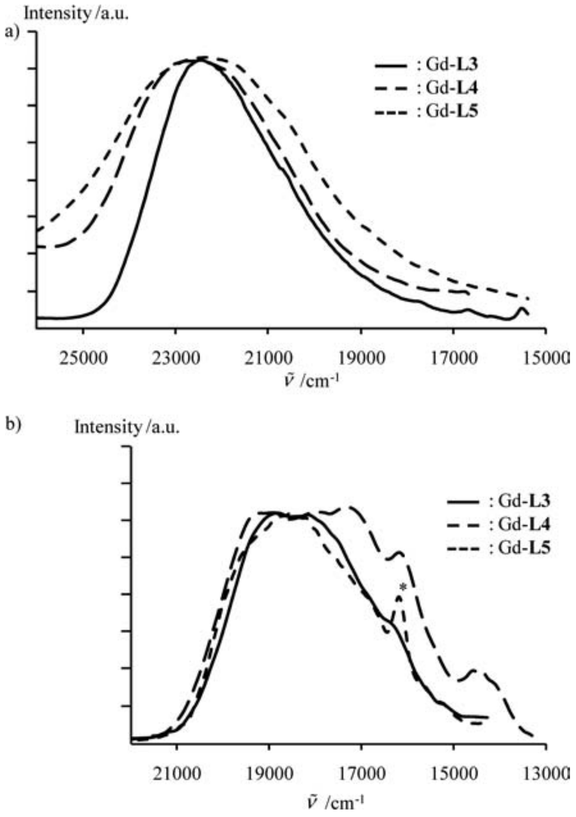

Figure 9. (a) Fluorescence and (b) phosphorescence (delay time after flash = 0.1 ms) spectra of $[Gd_2(\mathbf{L}\boldsymbol{k})(hfac)_6]$ (k = 3−5, solid state, 77 K, ν_{exc} = 28 650 cm^{-1}). The * indicates contamination with traces of highly emissive Eu(III) cations.

calculated with eq 8 (Table 2, column 12).

$$\frac{1}{\tau_L^{Gd}(F)} - \frac{1}{\tau_L^{Lk}(F)} = (k_r^F + k_{nr}^F + k_{ISC}^{Gd}) - (k_r^F + k_{nr}^F + k_{ISC}^{Lk})$$
$$= k_{ISC}^{Gd} - k_{ISC}^{Lk} \approx k_{ISC}^{Gd} \qquad (11)$$

Despite the non-negligible uncertainties affecting k_{ISC}^{Gd}, k_r^F, and η_{ISC} values because of the demanding experimental determination of very short $^1\pi\pi^*$ fluorescence lifetimes (Table 2, column 6), we conclude that the efficient ISC processes observed in $[Gd_2(\mathbf{L}\boldsymbol{k})(hfac)_6]$ ($\eta_{ISC} \approx$ 50−80%) have two concomitant origins. First, the well-known favorable heavy-atom and paramagnetic effects induced by the coordination of open-shell Ln(III) to aromatic ligands make the intersystem crossing rate constant k_{ISC}^{Gd} comparable with those of other nonradiative processes.[27] Second, the specific polarization of the aromatic system by the coordinated cation decreases the π-conjugation lengths A_π (Table 2, column 12) and the radiative rate constants k_r^F (eq 8; Table 2, column 7) in the Gd complexes

When Gd(III) is replaced with emissive Eu(III) in the complexes $[Eu_2(\mathbf{L}\boldsymbol{k})(hfac)_6]$, irradiation in the ligand-centered excited states at $\tilde{\nu}_{exc}$ = 28 650 cm^{-1} produces weak, ligand-centered fluorescence ($^1\pi\pi^* \rightarrow {}^1\pi\pi$) with traces of phosphorescence ($^3\pi\pi^* \rightarrow {}^1\pi\pi$) and an intense red signal arising from $\mathbf{L}\boldsymbol{k} \rightarrow$Eu energy transfer followed by Eu($^5D_1$) and Eu($^5D_0$)-centered luminescence (Figures 3 and 10). The intensities of the Eu($^5D_1 \rightarrow {}^7F_J$) transitions are extremely small compared to the luminescence arising from the Eu($^5D_0 \rightarrow {}^7F_J$) transitions,[11a] and the emission spectra are dominated by the hypersensitive forced electric dipolar Eu($^5D_0 \rightarrow {}^7F_2$) transition centered at 16 340 cm^{-1}. These two spectral characteristics are well-documented for low-symmetry tris-β-diketonate Eu(III) complexes (Figure 10).[23,25] With the naked eye, one immediately notices that the strong red luminescence obtained upon UV irradiation of solid samples is brightest for $[Eu_2(\mathbf{L4})(hfac)_6]$. This qualitative observation is substantiated by measurements of the global absolute quantum yields Φ_{Eu}^{L} (upon excitation of the ligand excited states and monitoring the Eu^{3+} emission) reaching 20.6(7)% for $[Eu_2(\mathbf{L4})(hfac)_6]$, 9.3(3)% for $[Eu_2(\mathbf{L3})(hfac)_6]$, and 9.2(3)% for $[Eu_2(\mathbf{L5})(hfac)_6]$ (solid state, 293 K, Table 4, entry 6). Using Einstein's result[35] for the spontaneous radiative emission rate A, given here as eq 12, $A_{MD,0}$ = 14.65 s^{-1} is obtained for the magnetic dipolar Eu($^5D_0 \rightarrow {}^7F_1$) transition. This calculation used n = 1.5 for the refractive index of the solid, and I_{tot}/I_{MD} was estimated as the ratio between the total integrated emission arising from the Eu($^5D_0$) level to the ^7F_J manifold and the integrated intensity of the magnetic dipolar Eu($^5D_0 \rightarrow {}^7F_1$) transition.[18a,22b]

$$k_r^{Eu} = A(\psi_J, \psi_{J'}) = A_{MD,0}\, n^3 (I_{tot}/I_{MD}) \qquad (12)$$

Integration of the corrected luminescence spectra recorded for $[Eu_2(\mathbf{L}\boldsymbol{k})(hfac)_6]$ (Figure 10) gives $17.5 \le I_{tot}/I_{MD} \le 18.6$ (Table 4, entry 1), which translates into comparable radiative rate constants $0.86 \le k_r^{Eu} \le 0.92$ ms^{-1} for the three complexes (Table 4, entry 2). Combining these results with the experimental Eu($^5D_0$) lifetimes (Table 4, entry 3) provides efficient intrinsic quantum yields Φ_{Eu}^{Eu} (eq 3, Table 4, entry 4), whose magnitudes increase smoothly along the series $\Phi_{Eu}^{Eu}([Eu_2(\mathbf{L3})(hfac)_6]) = 0.68(2) < \Phi_{Eu}^{Eu}([Eu_2(\mathbf{L4})(hfac)_6]) = 0.76(2) < \Phi_{Eu}^{Eu}([Eu_2(\mathbf{L5})(hfac)_6]) = 0.95(2)$, a trend which contrasts with that found for the global quantum yields Φ_{Eu}^{L} (Table 4, entry 6), but in line with Φ_{Eu}^{Eu}([Eu(pybox)(hfac)$_3$] recently determined in acetonitrile at 293 K.[36] Application of eq 7 yields the sensitization

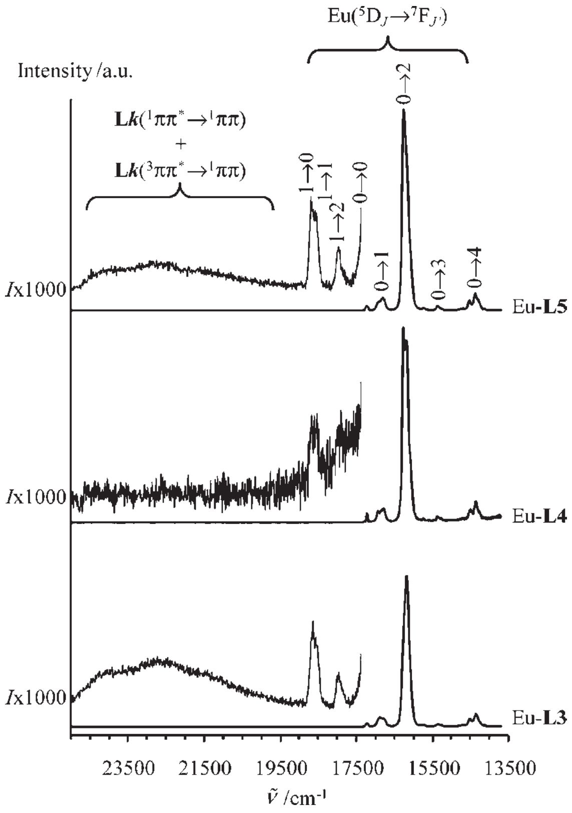

Figure 10. Luminescence emission spectra for $[\mathrm{Eu_2}(\mathbf{L}\boldsymbol{k})(\mathrm{hfac})_6]$ (k = 3−5, solid state, 293 K, ν_{exc} = 28 650 $\mathrm{cm^{-1}}$).

Table 4. Experimental Global ($\boldsymbol{\Phi^{\mathrm{L}}_{\mathrm{Eu}}}$) and Intrinsic ($\boldsymbol{\Phi^{\mathrm{Eu}}_{\mathrm{Eu}}}$) Quantum Yields, Luminescence Lifetimes ($\boldsymbol{\tau^{\mathrm{Eu}}}$, $\boldsymbol{\tau_{\mathrm{L}}{}^{\mathrm{Eu}}(\mathrm{P})}$), Calculated Energy Migration Efficiencies ($\boldsymbol{\eta_{\mathrm{ISC}}}$, $\boldsymbol{\eta^{\mathrm{L\to Ln}}_{\mathrm{en.tr.}}(\mathrm{P})}$), and Rate Constants ($\boldsymbol{k^{\mathrm{Eu}}_{\mathrm{r}}}$, $\boldsymbol{k^{\mathrm{Eu}}_{\mathrm{nr}}}$, $\boldsymbol{k^{\mathrm{tot}}_{\mathrm{en.tr.}}}$, $\boldsymbol{k^{\mathrm{P}}_{\mathrm{r}} + k^{\mathrm{P}}_{\mathrm{nr}}}$, $\boldsymbol{k_{\mathrm{ISC}}}$) for $\boldsymbol{[\mathrm{Eu_2}(\mathrm{L}k)(\mathrm{hfac})_6]}$ in the Solid State at 293 K

	$[\mathrm{Eu_2}(\mathbf{L3})$ $(\mathrm{hfac})_6]$	$[\mathrm{Eu_2}(\mathbf{L4})$ $(\mathrm{hfac})_6]$	$[\mathrm{Eu_2}(\mathbf{L5})$ $(\mathrm{hfac})_6]$
Eu-Centered Luminescence			
$I_{\mathrm{tot}}/I_{\mathrm{MD}}$[a]	17.5(3)	18.2(3)	18.6(3)
$k^{\mathrm{Eu}}_{\mathrm{r}}/\mathrm{ms^{-1}}$ (eq 12)	0.86(2)	0.90(2)	0.92(2)
τ^{Eu}/ms	0.88(4)	0.83(15)	1.06(16)
$\Phi^{\mathrm{Eu}}_{\mathrm{Eu}}$ (eq 3)	0.68(2)	0.76(2)	0.95(2)
$k^{\mathrm{Eu}}_{\mathrm{nr}}/\mathrm{ms^{-1}}$ (eq 3)	0.21(1)	0.23(4)	0.031(3)
Global Quantum Yield and Sensitization Efficiency			
$\tau^{\mathrm{L}}_{\mathrm{Eu}}$	0.092(3)	0.206(7)	0.093(3)
η_{ISC}, $\eta^{\mathrm{L\to Ln}}_{\mathrm{en.tr.}}(\mathrm{P})$ (eq 7)	0.122(7)	0.28(5)	0.096(8)
Energy Migration and Associated Rate Constants (Method 1)[b]			
η_{ISC}[c]	0.60(3)	0.6(1)	0.9(5)
$\eta^{\mathrm{L\to Ln}}_{\mathrm{en.tr.}}(\mathrm{P})$ (eq 7)	0.20(2)	0.47(14)	0.11(6)
$k^{\mathrm{tot}}_{\mathrm{en.tr.}}/\mathrm{ms^{-1}}$ (eq 13)	2.1(3)	5.5(2.3)	0.9(7)
$k^{\mathrm{P}}_{\mathrm{r}}+k^{\mathrm{P}}_{\mathrm{nr}}/\mathrm{ms^{-1}}$	8.1(5)	6.3(8)	7.1(3)
Energy Migration and Associated Rate Constants (Method 2)[d]			
$\tau^{\mathrm{Eu}}_{\mathrm{L}}(\mathrm{P})$/ms	0.10(1)	0.10(3)	0.11(1)
$k^{\mathrm{tot}}_{\mathrm{en.tr.}}/\mathrm{ms^{-1}}$ (eq 15)	2(1)	4(3)	2.0(9)
$\eta^{\mathrm{L\to Ln}}_{\mathrm{en.tr.}}(\mathrm{P})$(eq 16)	0.19(2)	0.38(12)	0.22(2)
η_{ISC} (eq 7)	0.65(8)	0.7(3)	0.44(6)
$k_{\mathrm{ISC}}/\mathrm{ns^{-1}}$ (eq 4)	10.8(1.5)	11(5)	16(9)

[a] Ratio between the total integrated emission for the $\mathrm{Eu(^5D_0)}$ level to the ^7F_J manifold and the integrated intensity of the magnetic dipolar $\mathrm{Eu(^5D_0 \to {}^7F_1)}$ transition. [b] A schematic illustration of these numerical data is shown in Figure S13. [c] Taken from Table 2 for the analogous complexes $[\mathrm{Gd_2}(\mathbf{L}\boldsymbol{k})(\mathrm{hfac})_6]$. [d] A schematic illustration of these numerical data is shown in Figure S14.

efficiency $\eta_{\mathrm{sens}} = \eta_{\mathrm{ISC}}\eta^{\mathrm{L\to Ln}}_{\mathrm{en.tr.}}(\mathrm{P}) = \Phi^{\mathrm{L}}_{\mathrm{Eu}}/\Phi^{\mathrm{Eu}}_{\mathrm{Eu}}$, which is twice as large for $[\mathrm{Eu_2}(\mathbf{L4})(\mathrm{hfac})_6]$ (0.28(5)) as for $[\mathrm{Eu_2}(\mathbf{L3})(\mathrm{hfac})_6]$ (0.122(7)) or $[\mathrm{Eu_2}(\mathbf{L5})(\mathrm{hfac})_6]$ (0.096(8), Table 4, entry 7). Considering that the values of η_{ISC} estimated for the respective Gd(III) complexes also hold for the Eu(III) complexes (Table 4, entry 8), we deduce values for $\eta^{\mathrm{L\to Ln}}_{\mathrm{en.tr.}}(\mathrm{P}) = \eta_{\mathrm{sens}}/\eta_{\mathrm{ISC}}$ (see Table 4, entry 9). If we assume that the $\mathbf{L}\boldsymbol{k}(^3\pi\pi^*)\to$Eu(III) energy-transfer process is the only additional perturbation affecting the deactivation of $^3\pi\pi^*$ upon replacement of Gd(III) with Eu(III) in $[\mathrm{Ln_2}(\mathbf{L}\boldsymbol{k})(\mathrm{hfac})_6]$, the assumption $k^{\mathrm{P}}_{\mathrm{r}} + k^{\mathrm{P}}_{\mathrm{nr}} = 1/\tau^{\mathrm{Gd}}_{\mathrm{L}}(\mathrm{P})$ (Table 4, entry 11) is valid, and eq 5 transforms into eq 13, from which the global rate constants for energy transfer $k^{\mathrm{tot}}_{\mathrm{en.tr.}}$ can be estimated (Table 4, entry 10).

$$\eta^{\mathrm{L\to Ln}}_{\mathrm{en.tr.}}(\mathrm{P}) = \frac{k^{\mathrm{tot}}_{\mathrm{en.tr.}}}{k^{\mathrm{P}}_{\mathrm{r}} + k^{\mathrm{P}}_{\mathrm{nr}} + k^{\mathrm{tot}}_{\mathrm{en.tr.}}}$$

$$\Rightarrow k^{\mathrm{tot}}_{\mathrm{en.tr.}} = (k^{\mathrm{P}}_{\mathrm{r}} + k^{\mathrm{P}}_{\mathrm{nr}})\left(\frac{\eta^{\mathrm{L\to Ln}}_{\mathrm{en.tr.}}(\mathrm{P})}{(1 - \eta^{\mathrm{L\to Ln}}_{\mathrm{en.tr.}}(\mathrm{P}))}\right)$$

$$= \frac{1}{\tau^{\mathrm{Gd}}_{\mathrm{L}}(\mathrm{P})}\left(\frac{\eta^{\mathrm{L\to Ln}}_{\mathrm{en.tr.}}(\mathrm{P})}{(1 - \eta^{\mathrm{L\to Ln}}_{\mathrm{en.tr.}}(\mathrm{P}))}\right) \qquad (13)$$

Figures 11, S13, and S14 summarize the efficiency and rate constant for each step contributing to the ligand-centered sensitization processes in the three complexes $[\mathrm{Eu_2}(\mathbf{L}\boldsymbol{k})(\mathrm{hfac})_6]$ (k = 3−5). Focusing on the average numerical values, we conclude that the $\mathbf{L}\boldsymbol{k}(^3\pi\pi^*)\to$Eu(III) energy-transfer process represents the bottleneck which limits the global quantum yield, whatever the choice of the substituents. However, the rate-limiting step is fastest for the difluorophenyl spacer found in $[\mathrm{Eu_2}(\mathbf{L4})(\mathrm{hfac})_6]$. Because the Fermi golden rule implies that the probability W_{DA} of any resonant energy transfer depends on the spectral overlap integral Ω_{DA} between the absorption spectrum of the acceptor **A** and the emission spectrum of the donor **D** (eq 14),[16d,20] we hypothesize that the global blue-shifted ligand-centered emission observed for the fluorinated complex $[\mathrm{Eu_2}(\mathbf{L4})(\mathrm{hfac})_6]$ causes a larger spectral overlap, with $\mathrm{Eu(^5D_2)}$ and/or $\mathrm{Eu(^5D_1)}$ levels of Eu(III) acting as accepting levels (Figure 11).[48] We cannot, however, completely exclude some concomitant changes in the perturbation terms $|\langle \mathbf{DA}^*|\mathrm{H'}|\mathbf{D}^*\mathbf{A}\rangle|^2$ due to specific stereoelectronic characteristics of the ground and excited states in $[\mathrm{Eu_2}(\mathbf{L}\boldsymbol{k})(\mathrm{hfac})_6]$.

$$W_{\mathrm{DA}} = (2\pi/\hbar)|\langle \mathbf{DA}^*|\mathrm{H'}|\mathbf{D}^*\mathbf{A}\rangle|^2\Omega_{\mathrm{DA}} \qquad (14)$$

The propagation of uncertainties[49] prevents a deeper interpretation of η_{ISC} and $\eta^{\mathrm{L\to Ln}}_{\mathrm{en.tr.}}(\mathrm{P})$, especially for $[\mathrm{Eu_2}(\mathbf{L5})(\mathrm{hfac})_6]$, by using the latter approach (termed method 1 in Table 4, entries 8 and 9). This limitation can be tentatively overcome when the intensity of the residual ligand-centered triplet-state phosphorescence in $[\mathrm{Eu_2}(\mathbf{L}\boldsymbol{k})(\mathrm{hfac})_6]$ is strong enough to allow the reliable experimental determination of its characteristic

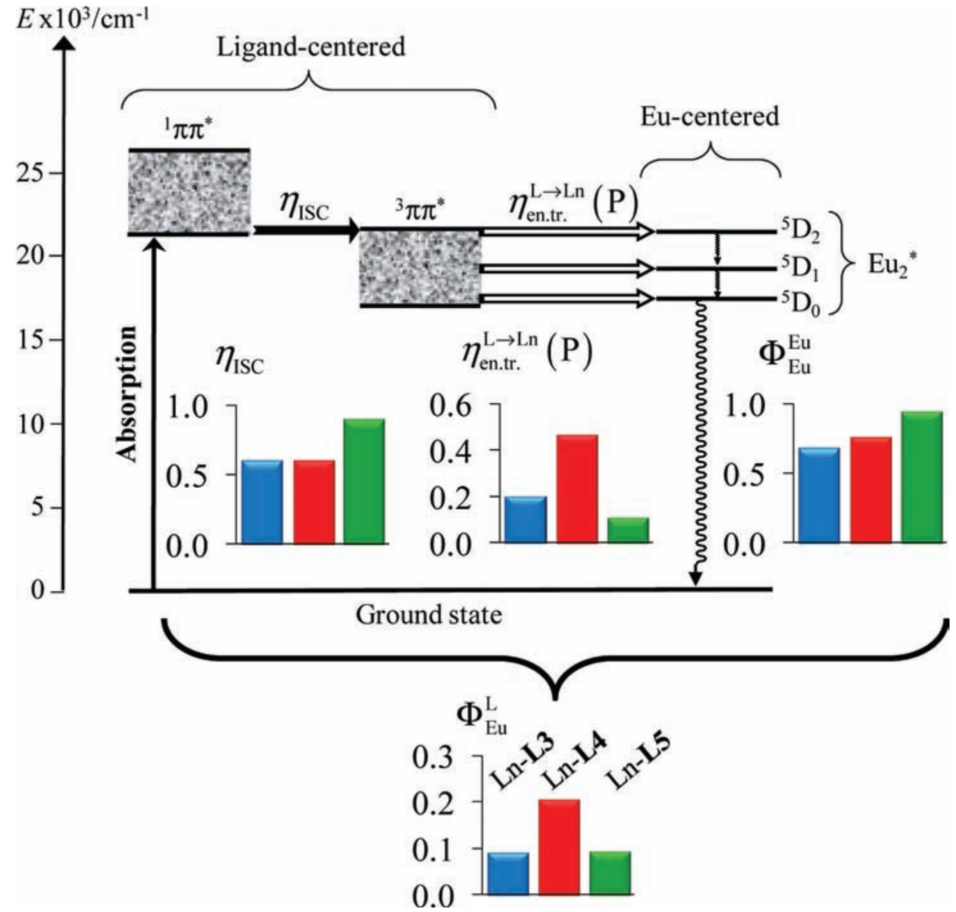

Figure 11. Jablonski diagram established for $[Eu_2(\mathbf{L}\boldsymbol{k})(hfac)_6]$ (k = 3−5) and efficiencies of intersystem crossings (η_{ISC}), energy transfers ($\eta_{en.tr.}^{L\to Eu}(P)$), intrinsic quantum yields (Φ_{Eu}^{Eu}), and global quantum yields (Φ_{Eu}^{L}) for the global ligand-mediated sensitization of Eu(III) (solid state, 293 K). Color codes: $[Eu_2(\mathbf{L3})(hfac)_6]$ = blue, $[Eu_2(\mathbf{L4})(hfac)_6]$ = red, and $[Eu_2(\mathbf{L5})(hfac)_6]$ = green.

lifetime $\tau_L^{Eu}(P)$ (Table 4, entry 12). Relying on the usual assumption that the $\mathbf{L}\boldsymbol{k}(^3\pi\pi^*)\to$Eu(III) energy-transfer process (characterized by $k_{en.tr.}^{tot}$ in Figure 3) is the only additional perturbation affecting the deactivation of $^3\pi\pi^*$ upon replacement of Gd(III) with Eu(III) in $[Ln_2(\mathbf{L}\boldsymbol{k})(hfac)_6]$, $k_{en.tr.}^{tot}$ (Table 4, entry 13) can be deduced from eq 15 (termed method 2 in Table 4; $\tau_L^{Gd}(P)$ (Table 1, column 7) and $\tau_L^{Eu}(P)$ (Table 4, entry 12) are the experimental luminescence lifetimes for the ligand-centered triplet state in the complexes with Gd(III) and Eu(III), respectively). $\eta_{en.tr.}^{L}(P)$ can then be estimated with eq 16 (Table 4, entry 14).

$$k_{en.tr.}^{tot} = (k_r^P + k_{nr}^P + k_{en.tr.}^{tot}) - (k_r^P + k_{nr}^P) = \frac{1}{\tau_L^{Eu}(P)} - \frac{1}{\tau_L^{Gd}(P)} \tag{15}$$

$$\eta_{en.tr.}^{L\to Ln}(P) = k_{en.tr.}^{tot}\,\tau_L^{Eu}(P) = 1 - \frac{\tau_L^{Eu}(P)}{\tau_L^{Gd}(P)} \tag{16}$$

The values for $\eta_{ISC} = \eta_{sens}/\eta_{en.tr.}^{L\to Ln}(P)$ (Table 4, entry 15) are obtained from the known sensitization factors η_{sens} (Table 4, entry 7) without having to record sub-nanosecond fluorescence lifetimes for $[Gd_2(\mathbf{L}\boldsymbol{k})(hfac)_6]$. Reasonably assuming that η_{ISC} is identical in the dinuclear Gd(III) and Eu(III) complexes, we can calculate k_{ISC} by using eq 4 (Table 4, entry 16). Both approaches converge toward the same average values for the rate constants within experimental errors (Figures 11, S13, and S14), and a close scrutiny of the uncertainties shows that the accuracies of the techniques are complementary.

■ EXPERIMENTAL SECTION

Chemicals were purchased from Strem, Acros, Fluka AG, and Aldrich and used without further purification unless otherwise stated. The synthesis of the starting compound **1** is described in the Supporting Information (Scheme S1). The hexafluoroacetylacetonate salts $[Ln(hfac)_3\text{-}C_8H_{12}O_3]$ were prepared from the corresponding oxide (Aldrich, 99.99%, appendix 3 in the Supporting Information).[38] Acetonitrile and dichloromethane were distilled over calcium hydride. Merck 60 F_{254} silica gel plates were used for thin-layer chromatography (TLC), and Fluka silica gel 60 (0.04−0.063 mm) or Acros neutral activated alumina (0.050−0.200 mm) was used for preparative column chromatography.

Preparation of 2. A 20 mL THF solution of 1,4-dibromobenzene (4.72 g, 20 mmol) was added dropwise to a suspension of magnesium shavings (1.06 g, 43.6 mmol) in dry THF (10 mL) under an inert atmosphere. The mixture was refluxed for 24−48 h until the appearance of a gray precipitate. Trimethylborate (5 mL, 4.66 g, 44.8 mmol) in THF (50 mL) was added and the mixture refluxed for 2 h. The white gel was poured into aqueous hydrochloric acid (2 M, 200 mL) and stirred for 1 h at room temperature. The clear solution was extracted with diethyl ether (4 × 200 mL), and the combined organic phases were dried (Na_2SO_4), filtered, and evaporated to dryness. Recrystallization from hot water

(200 mL) gave **2** as transparent crystals (1.6 g, 9.6 mmol, 48%). ^{1}H NMR (acetone-d_6; 400 MHz): δ = 7.86 (s, 4H), 7.13 (s, 4H). ESI-MS (negative mode/CH_3OH): m/z 165.3 ([M−H]$^-$), 179.1 ([M+CH_3OH−H]$^-$).

Preparation of 3. 1,4-Dimethoxybenzene (1.38 g, 10.0 mmol) was dissolved in 20 mL of dry hexane, and the solution was kept at 0 °C. *n*BuLi (37.5 mL, 1.6 M in hexane, 60.0 mmol) and TMEDA (4.5 mL, 30.0 mmol) were slowly added to the solution during 30 min. The resulting yellow solution was stirred at room temperature for 48 h under an inert atmosphere and cooled at 0 °C. $B(OMe)_3$ (7.6 mL, 66 mmol) was added via a syringe under vigorous stirring and produced a white precipitate. After 2 h, the turbid solution was evaporated to dryness. The white solid was poured into aqueous hydrochloric acid (1 M, 200 mL). The clear solution was extracted with diethyl ether (4 × 200 mL), and the combined organic phases were dried (Na_2SO_4), filtered, and evaporated to dryness to give **3** as a white powder (0.70 g, yield = 31%). ^{1}H NMR (DMSO-d_6; 400 MHz): δ = 7.15 (s, 2H), 3.77 (s, 6H). ESI-MS (positive mode/CH_3OH): m/z 226.4 ([M+H]$^+$).

Preparation of 4. 1,4-Dibromo-2,5-difluorobenzene (1.23 g, 4.7 mmol) and Pd^{II}dppfCl$_2$ (112 mg, 0.153 mmol, dppf =1,1′-bis-(diphenylphosphino)ferrocene) were dissolved in degassed DMF (40 mL). The resulting red solution was slowly transferred via a cannula into a Schlenk vessel charged with bis(pinacolato)diboron (2.54 g, 10.0 mmol) and potassium acetate (2.03 g, 20.5 mmol). The resulting red mixture was heated at 80 °C for 24 h. The cooled black solution was partitioned between dichloromethane (100 mL) and half-saturated aqueous NaCl (100 mL). The organic layer was separated, washed with water (2 × 100 mL), dried ($MgSO_4$), and evaporated. The black solid was loaded in a Kugelrohr apparatus and heated at 140 °C under vacuum to give white crystals of **4** (170 mg; yield = 10%). ^{1}H NMR ($CDCl_3$; 400 MHz): δ = 7.33 (t, J_{H-F} = 6.6 Hz, 2H), 1.35 (s, 24H). ESI-MS (positive mode/CH_3OH): m/z 385.3 ([M+H_3O]$^+$).

Preparation of L3. Compounds **1** (0.89 g, 2.0 mmol) and **2** (166 mg, 1.0 mmol) were dissolved in dioxane/ethanol (30 mL:20 mL) containing cesium fluoride (1.37 g, 9 mmol) under an inert atmosphere. The turbid solution was degassed by nitrogen bubbling during 20 min. $Pd(PPh_3)_4$ (100 mg, 0.09 mmol) was added, and the resulting yellow solution was stirred for 20 min at room temperature and then refluxed for 24 h. After evaporation to dryness, the solid residue was partitioned between dichloromethane (150 mL) and half-saturated aqueous NaCl (200 mL). The aqueous phase was separated and extracted with dichloromethane (200 mL), and the combined organic phases were dried (Na_2SO_4), filtered, and evaporated to dryness. The crude brown solid was purified by column chromatography (silica gel, CH_2Cl_2:CH_3OH:NEt_3 = 99.5:0:0.5→96.5:3:0.5) to give a pale yellow solid, which was crystallized from dichloromethane:ethanol to give **L3** as a pale yellow powder (0.58 g, 0.71 mmol, yield = 71%). ^{1}H NMR ($CDCl_3$; 400 MHz): δ = 1.40 (t, ^3J = 7 Hz, 3H), 1.42 (t, ^3J = 7 Hz, 3H), 4.83 (q, ^3J = 7 Hz, 2H), 4.85 (q, ^3J = 7 Hz, 2H), 7.38 (multiplet, 4H), 7.51 (dd, ^3J = 6 Hz, ^4J = 2 Hz, 2H), 7.58 (d, ^3J = 8 Hz, 2H), 7.72 (dd, ^3J = 7 Hz, ^4J = 1 Hz, 2H), 7.83 (s, 4H), 7.91 (dd, ^3J = 7 Hz, ^4J = 1 Hz, 2H), 8.10 (t, ^3J = 7 Hz, 2H), 8.18 (d, ^4J = 1 Hz, 2H), 8.39 (d, ^3J = 8 Hz, 2H), 8.41 (d, ^3J = 8 Hz, 2H). ^{13}C NMR ($CDCl_3$, 101 MHz): δ = 150.64, 150.18, 150.04, 149.98, 143.67, 143.05, 140.39, 138.23, 136.16, 136.09, 135.70, 127.94, 125.87, 125.81, 123.66, 123.43, 122.90, 120.47, 118.62, 110.60, 110.37, 40.09, 39.91, 15.60, 15.54. ESI-MS (positive mode/CH_3OH): m/z 405.5 ([**L3**+2H]$^{2+}$), 810 ([**L3**+H]$^+$). Elemental analyses: calcd for $C_{52}H_{44}N_{10}\cdot H_2O$ C 75.52, H 5.60, N 16.94; found C 75.60, H 5.47, N 16.72.

Preparation of L4. Compounds **1** (311 mg, 0.70 mmol) and **4** (106 mg, 0.29 mmol) were dissolved in dioxane/ethanol (50 mL:30 mL) containing cesium fluoride (200 mg, 1.4 mmol) under an inert atmosphere. The turbid solution was degassed by nitrogen bubbling for 20 min. $Pd(PPh_3)_4$ (50 mg, 0.04 mmol) was added, and the resulting yellow solution was stirred for 20 min at room temperature and then refluxed for 24 h. After evaporation to dryness, the solid residue was partitioned between dichloromethane (150 mL) and half-saturated aqueous NaCl (200 mL). The aqueous phase was separated and extracted with dichloromethane (200 mL), and the combined organic phases were dried (Na_2SO_4), filtered, and evaporated to dryness. The crude brown solid was purified by column chromatography (silica gel, CH_2Cl_2:CH_3OH:NEt_3 = 99.5:0:0.5→96.5:3:0.5) to give a yellow solid, which was crystallized from dichloromethane:petroleum ether to give **L4** as an off-white powder (110 mg, 0.13 mmol, yield = 45%). ^{1}H NMR (400 MHz; $CDCl_3$): δ = 1.39 (t, ^3J = 7.5 Hz, 3H), 1.42 (t, ^3J = 7.5 Hz, 3H), 4.82 (q, ^3J = 7.4 Hz, 2H), 4.85 (q, ^3J = 7.4 Hz, 2H), 7.38 (m., 2H), 7.40 (t, $^3J_{H-F}$=$^4J_{H-F}$ = 8.6 Hz, 1H), 7.51 (dd, ^3J = 6.3 Hz, ^4J = 1.5 Hz, 1H), 7.59 (d, ^3J = 8.3 Hz, 1H), 7.64 (d, ^3J = 8.3 Hz, 1H), 7.89 (dd, ^3J = 7.0 Hz, ^4J = 2.1 Hz, 1H), 8.09 (t, ^3J = 8.0 Hz, 1H), 8.12 (s, 1H), 8.39 (dd, ^3J = 7.9 Hz, ^4J = 2.0 Hz, 2H). ESI-MS: m/z 423.4 ([**L4**+2H]$^{2+}$), 845.3 ([**L4**+H]$^+$). ^{13}C NMR (101 MHz $CDCl_3$): δ = 147.14, 146.51, 146.24, 139.95, 139.72, 135.25, 133.16, 133.08, 127.84 ($^1J_{C-F}$ = 350.2 Hz, $^4J_{C-F}$ = 10.1 Hz), 127.02, 126.87 ($^2J_{C-F}$ = $^3J_{C-F}$ = 11.6 Hz), 123.60, 123.49, 122.53, 121.45, 120.72, 118.77, 118.40, 116.01 ($^2J_{C-F}$ = $^3J_{C-F}$ = 17.5 Hz), 108.95, 108.86, 42.43, 42.24, 19.24, 19.19. Elemental analyses: calcd for $C_{52}H_{42}N_{10}F_2$, C 73.91, H 5.01, N 16.58; found C 72.66, H 4.70, N 15.95.

Preparation of L5. Compounds **1** (0.86 g, 1.94 mmol) and **3** (218 mg, 0.97 mmol) were dissolved in dioxane/ethanol (30 mL:20 mL) containing cesium fluoride (1.37 g, 9 mmol) under an inert atmosphere. The turbid solution was degassed by nitrogen bubbling for 20 min. $Pd(PPh_3)_4$ (150 mg, 0.13 mmol) was added, and the resulting yellow solution was stirred for 20 min at room temperature and then refluxed for 24 h. After evaporation to dryness, the solid residue was partitioned between dichloromethane (150 mL) and half-saturated aqueous NaCl (200 mL). The aqueous phase was separated and extracted with dichloromethane (200 mL), and the combined organic phases were dried (Na_2SO_4), filtered, and evaporated to dryness. The crude brown solid was purified by column chromatography (silica gel, CH_2Cl_2:CH_3OH:NEt_3 = 99.5:0:0.5→96.5:3:0.5) to give a yellow solid, which was crystallized from dichloromethane:ethanol to give **L5** as a microcrystalline yellow powder (0.42 g, 0.48 mmol, yield = 50%). ^{1}H NMR (400 MHz $CDCl_3$): δ = 1.39 (t, ^3J = 7 Hz, 3H), 1.42 (t, ^3J = 7 Hz, 3H), 3.86 (s, 3H), 4.82 (q, ^3J = 7 Hz, 2H), 4.84 (q, ^3J = 7 Hz, 2H), 7.15 (s, 2H), 7.38 (m., 4H), 7.51 (dd, ^3J = 6 Hz, ^4J = 2 Hz, 2H), 7.56 (d, ^3J = 8 Hz, 2H), 7.69 (dd, ^3J = 7 Hz, ^4J = 1 Hz, 2H), 7.89 (dd, ^3J = 7 Hz, ^4J = 1 Hz, 2H), 8.08 (t, ^3J = 7 Hz, 2H), 8.14 (d, ^4J = 1 Hz, 2H), 8.37 (d, ^3J = 8 Hz, 2H), 8.39 (d, ^3J = 8 Hz, 2H). ^{13}C NMR (101 MHz, $CDCl_3$): δ = 150.90, 150.46, 150.18, 150.15, 150.04, 143.15, 143.08, 138.25, 136.13, 135.41, 133.43, 130.68, 125.81, 123.68, 122.92, 121.20, 120.51, 115.28, 110.39, 109.85, 56.60, 40.06, 39.97, 15.66, 15.58. ESI-MS (positive mode/CH_3OH): m/z 435.6 ([**L5**+2H]$^{2+}$), 869.3 ([**L5**+H]$^+$). Elemental analyses: calcd for $C_{54}H_{48}N_{10}O_2\cdot 0.15CHCl_3$, C 73.30, H 5.47, N 15.79; found C 73.35, H 5.23, N 15.66.

Preparation of Complexes [Ln_2(L*k*)(hfac)$_6$] (*k* = 3−5). In a typical procedure, 0.05 mmol (ca. 40−45 mg) of [Ln(hfac)$_3$diglyme] was dissolved in chloroform (2 mL) and then added to 0.024 mmol of ligand (ca. 20 mg) in chloroform (1 mL). For ligands **L3** and **L5**, precipitation occurred immediately. For ligand **L4**, the solution was cooled for 2 h at −20 °C until precipitation. Complexes were collected as pale yellow microcrystalline powders by filtration and dried under vacuum at 70 °C (yields = 50−90%, Table S2). Monocrystals suitable for X-ray diffraction were obtained by reacting 0.015 mmol of [Ln(hfac)$_3$diglyme] in acetonitrile (2 mL) with 0.006 mmol of ligand in chloroform (0.2 mL). Slow evaporation or slow diffusion of diethyl ether yielded yellow prisms.

Spectroscopic Measurements. ^{1}H, ^{19}F, and ^{13}C NMR spectra were recorded at 298 K on Bruker Avance 400 MHz and Bruker DRX 300 MHz spectrometers. Chemical shifts are given in ppm with respect to TMS. Pneumatically assisted electrospray ionization mass spectra

(ESI-MS) were recorded from 10^{-4} M solutions on an Applied Biosystems API 150EX LC/MS system equipped with a Turbo Ionspray source. Elemental analyses were performed by Dr. H. Eder or K. L. Buchwalder from the Microchemical Laboratory of the University of Geneva. Electronic absorption spectra in the UV–vis region were recorded at 20 °C from solutions in CH_2Cl_2 with a Perkin-Elmer Lambda 900 spectrometer using quartz cells of 10 or 1 mm path length. Some of the excitation and emission spectra were recorded on a Perkin-Elmer LS-50B spectrometer equipped for low-temperature measurements. The quantum yields Φ for the free ligands in solution were recorded through the relative method with respect to quinine sulfate 6.42×10^{-6} M in 0.05 M H_2SO_4 (refractive index 1.338 and quantum yield 0.546)[37] and calculated using the equation

$$\frac{\Phi_x}{\Phi_r} = \frac{A_r(\tilde{\nu})I_r(\tilde{\nu})n_x^2 D_x}{A_x(\tilde{\nu})I_x(\tilde{\nu})n_r^2 D_r}$$

where x refers to the sample and r to the reference; A is the absorbance, $\tilde{\nu}$ the excitation wavenumber used, I the intensity of the excitation light at this energy, n the refractive index, and D the integrated emitted intensity. Luminescence spectra in the visible region were measured using a Jobin Yvon–Horiba Fluorolog-322 spectrofluorimeter equipped with a Hamamatsu R928. Spectra were corrected for both excitation and emission responses (excitation lamp, detector, and both excitation and emission monochromator responses). Quartz tube sample holders were employed. Quantum yield measurements of the solid-state samples were measured on quartz tubes with the use of an integration sphere developed by Frédéric Gumy and Jean-Claude G. Bünzli (Laboratory of Lanthanide Supramolecular Chemistry, École Polytechnique Féderale de Lausanne, Lausanne, Switzerland) commercialized by GMP S.A. (Renens, Switzerland). For long luminescence lifetimes, triplet states (on Eu^{3+} and Gd^{3+} complexes) and lanthanide-centered luminescence lifetimes were measured at 293 K using either a Nd:YAG Continuum Powerlite 8010 laser or a Quantel YG 980 (354 nm, third harmonic) as the excitation source. Emission was collected at a right angle to the excitation beam, and wavelengths were selected by either a Spectral Products CM 110 1/8 m monochromator or interferential filters. The signal was monitored by a Hamamatsu R928 photomultiplier tube and collected on a 500 MHz band-pass digital oscilloscope (Tektronix TDS 724C). Experimental luminescence decay curves were treated with Origin 7.0 software using exponential fitting models. Three decay curves were collected on each sample, and reported lifetimes are an average of at least two successful independent measurements. For rapid decays analysis (singlet states), the time-resolved luminescence decay kinetics was measured using the time-correlated single-photon-counting (TCSPC) technique. Samples were excited with the frequency-doubled output (centered at ~335 nm) of a synchronously pumped cavity-dumped dye laser (model 599, Coherent, Santa Clara, CA) using 4-(dicyanomethylene)-2-methyl-6-(4-dimethylaminostyryl)-4*H*-pyran (DCM) as the gain medium; emission from the sample was collected at different wavelengths using a monochromator. The instrument response function had a full width at half-maximum (fwhm) of ~40 ps. A 1 cm path length quartz cuvette was used for all the time-resolved measurements in solutions. Measurements with solid samples were performed in a quartz capillary. All measurements were performed at room temperature. Experiments were performed with a 1 MHz laser repetition rate. Lifetime decay traces were fitted by an iterative reconvolution method with IBH DAS 6 decay analysis software.

X-ray Crystallography. Crystal data, intensity measurements, and structure refinements for $[Yb_2(\mathbf{L3})(hfac)_6]$ (**1**), $[Y_2(\mathbf{L3})(hfac)_6]$ (**2**), $[Yb_2(\mathbf{L4})(hfac)_6]$ (**3**), and $[Eu_2(\mathbf{L5})(hfac)_6]$ (**4**) are collected in Table S3 (Supporting Information). All crystals were mounted on quartz fibers with protection oil. Cell dimensions and intensities were measured between 150 and 200 K on a Stoe IPDS diffractometer with graphite-monochromated Mo Kα radiation ($\lambda = 0.71073$ Å). Data were corrected for Lorentz and polarization effects and for absorption. The structures were solved by direct methods (SIR97).[50] All other calculation were performed with ShelX97[51] systems and ORTEP[52] programs. CCDC-822835–CCDC-822838 contain the crystallographic data for **1**–**4** (also available as Supporting Information). The files can be obtained free of charge via www.ccdc.cam.ac.uk/conts/retrieving.html or from the Cambridge Crystallographic Data Centre, 12 Union Rd., Cambridge CB2 1EZ, UK; fax (+ 44) 1223-336-033, or deposit@ccdc.cam.ac.uk.

Comments on the Crystal Structure of $[Yb_2(L3)(hfac)_6]$ (1) and $[Y_2(L3)(hfac)_6]$ (2). These complexes were isostructural. $[Ln_2(\mathbf{L3})(hfac)_6]$ were located on a twofold axis passing through the central phenyl ring, leading to only one half of the complex in the asymmetric unit (Figure 7a). The crystal packing displayed channel voids along the [1 0 1] direction, where solvent molecules were highly disordered (Figure S15). Squeezed calculations were thus performed, and the solvent-free structures were refined. The presence of these channels may explain the loss of solvent during the measurement, which results in partial decomposition of the crystal and incomplete data collection. The CF_3 units of the counter-anions showed some disorder and were refined isotropically. Hydrogen atoms were calculated and refined with restraints on bond lengths and bond angles.

Comments on the Crystal Structure of $[Yb_2(L4)(hfac)_6]$ (3). $[Yb_2(\mathbf{L4})(hfac)_6]$ was located around an inversion center (in the center of the central phenyl ring), leading to only one half of the complex in the asymmetric unit (Figure 7b). One CF_3 unit (F5–F6–F7) was disordered (rotation) and was refined with identical isotropic displacement parameters on two sites with population parameters refined to PP = 0.54/0.46. H atoms were observed from the Fourier difference map and refined with restraints on bond lengths and bond angles.

Comments on the Crystal Structure of $[Eu_2(L5)(hfac)_6]$ (4). $[Eu_2(\mathbf{L5})(hfac)_6]$ was located around an inversion center (in the center of the central phenyl ring), leading to only one half of the complex in the asymmetric unit (Figure 7c). H atoms were observed from the Fourier difference map and refined with restraints on bond lengths and bond angles. All non-H atoms were refined anisotropically.

Computational Details. The lowest electronic excitations at the optimized geometry of the ligands were obtained by means of TD-DFT calculations.[53] The preliminary analyses of the excited-state properties were made to estimate the weighting of the HOMO–LUMO transitions, which indeed provided the dominant component to the excitation energy for the studied systems. We thus limited the discussions of the electronic state of the ligands to the HOMO and LUMO orbitals obtained from ground-state DFT calculations. All calculations were performed using the Turbomole package (version 6.1)[54] with the PBE functional.[55] Geometry optimization was carried out without symmetry constraints, using the def2-TZVP basis set. In geometry optimization, the following thresholds were applied: 10^{-6} hartree for energy difference and 10^{-3} hartree/bohr for the norm of the energy gradient. The HOMO–LUMO gap was calculated at the optimized geometry. The optimization started from the crystallographic structure. The dependence of the HOMO–LUMO gap on the torsion angle α between the 1,4-disubstituted phenyl spacer and the adjacent 5-benzimidazole rings (Figure S1, Supporting Information) was studied by a series of single-point calculations with all remaining degrees of freedom frozen.

■ CONCLUSION

Reactions of stoichiometric amounts of bis-tridentate ligands **L3**–**L5** with $[Ln(hfac)_3diglyme]$ in acetonitrile quantitatively give the anhydrous and poorly soluble dinuclear complexes $[Ln_2(\mathbf{L}\boldsymbol{k})(hfac)_6]$. While the limited affinity of the $Ln(hfac)_3$ moiety for the tridentate binding unit prevents the formation of more than 80% of the complex at the highest accessible concentrations (0.1–0.5 mM), X-ray diffraction data unambiguously demonstrate the formation of the expected single-stranded dumbbell-shaped complexes. In the solid state, one finds that two globular nine-coordinate [$N_3Ln(hfac)_3$] units are connected by a disubstituted phenyl ring and separated by 1.3−1.5 nm. Except for the slightly larger solubility of [Ln_2(**L4**)$(hfac)_6$], objective arguments for selecting one specific phenyl spacer for further development of a polymerization protocol rely on the specific photophysical properties of the luminescent Eu(III) complexes. Thorough characterization of the kinetic rate constants responsible for the indirect sensitization of Eu(III) in [Eu_2(**L*k***)$(hfac)_6$], within the frame of a simple triplet energy migration scheme, shows that both ligand-centered intersystem crossing ($\eta_{ISC} \approx 50-80\%$) and metal-centered luminescence ($\Phi_{Eu}^{Eu} = 68-95\%$) are efficient. These kinetic steps are not very sensitive to the nature of the substituents studied. In contrast, the ligand-to-metal energy transfer acts as the rate-limiting step ($\eta_{en.tr.}^{L\to Ln}(P) = 11-47\%$), and it is significantly affected by the choice of the substituents. Whatever the origin of the favorable effect brought by fluorine substitution in [Eu_2(**L4**)$(hfac)_6$], it is worth stressing here that the energy-transfer step is the only significant parameter amenable to tuning by minor substitutions of the central phenyl spacer in [Ln_2(**L*k***)$(hfac)_6$]. Though this conclusion is in line with innumerable previous reports, a safe assertion of it requires a comprehensive determination of all rate constants involved in the sensitization processes, as shown in Figure 11. The two complementary and general methods used in this contribution exploit the routine experimental determination of global (Φ_{Ln}^{L}) and intrinsic (Φ_{Ln}^{Ln}) quantum yields as a starting point. Method 1 focuses on the measurement of short $^1\pi\pi^*$ fluorescence lifetimes, and data obtained for the free ligand and for the corresponding Gd(III) complex are compared. The accuracy is strongly dependent on the quality of the ps→ns time scale lifetime data. Alternatively, method 2 relies on the determination of more easily accessible long $^3\pi\pi^*$ lifetimes and compares the data obtained for the Gd(III) and Eu(III) complexes. In this case, the accuracy is limited by the faint (if any) intensities detected for the residual $^3\pi\pi^* \to {}^1\pi\pi$ phosphorescence in the emissive Eu(III) complexes at room temperature. It is obvious that the simultaneous use of both methods will produce more reliable results, but systems which escape one approach, for instance [Ln_2(**L5**)$(hfac)_6$] because of the ultrashort fluorescence lifetime of the Gd(III) complex, can be still investigated following the alternative protocol.

ASSOCIATED CONTENT

Ⓢ **Supporting Information.** Details for the determination of stability constants (appendix 1) and for the correction of electronic absorption spectra (appendix 2); synthesis of starting materials (appendices 3 and 4); tables of ^{1}H NMR shifts, elemental analyses, crystal data, geometric parameters, and bond valences; figures showing DFT calculations, ^{1}H NMR spectra, electronic absorption and emission spectra, Jablonski diagrams, and crystal packing; CIF file containing X-ray crystallographic data for **1**−**4**. This material is available free of charge via the Internet at http://pubs.acs.org.

AUTHOR INFORMATION

Corresponding Author

claude.piguet@unige.ch; tomasz.wesolowski@unige.ch; stephane.petoud@cnrs-orleans.fr; dave@pitt.edu

ACKNOWLEDGMENT

Financial support from the Swiss National Science Foundation is gratefully acknowledged. D.H.W. and S.P. acknowledge support from the U.S. National Institutes of Health via NIH grant R21-EB008257-01A1, and D.H.W. acknowledges partial support from the National Science Foundation (CHE-0718755). S.P. acknowledges support in France from la Ligue contre le Cancer and from Institut National de la Santé et de la Recherche Médicale (INSERM). The work in France was carried out within the COST Action D38. K.A.G. acknowledges support from the Mary E. Warga Predoctoral Fellowship

REFERENCES

(1) (a) Binnemans, K. *Chem. Rev.* **2009**, *109*, 4283–4374. (b) Vigato, P. A.; Peruzzo, V.; Tamburini, S. *Coord. Chem. Rev.* **2009**, *253*, 1099–1201. (c) Brito, H. F.; Malta, O. M. L.; Felinto, M. C. F. C.; Teotonio, E. E. S. *The Chemistry of Metal Enolates*; John Wiley & Sons, Ltd.: New York, 2009; Chap. 3, pp 131−184.

(2) (a) Evans, R. C.; Douglas, P.; Winscom, C. J. *Coord. Chem. Rev.* **2006**, *250*, 2093–2126. (b) de Bettencourt-Dias, A. *Dalton Trans.* **2007**, 2229–2241. (c) Katkova, M. A.; Bochkarev, M. N. *Dalton Trans.* **2010**, *39*, 6599–6612.

(3) (a) Shunmugam, R.; Tew, G. N. *J. Polym. Sci. A: Polym. Chem.* **2005**, *43*, 5831–5843. (b) Shunmugam, R.; Tew, G. N. *J. Am. Chem. Soc.* **2005**, *127*, 13567–13572. (c) Lou, X.; Zhang, G.; Herrera, I.; Kinach, R.; Ornatsky, O.; Baranov, V.; Nitz, M.; Winnik, M. A. *Angew. Chem., Int. Ed.* **2007**, *46*, 6111–6114. (d) Balamurugan, A.; Reddy, M. L. P.; Jayakannan, M. *J. Phys. Chem. B* **2009**, *113*, 14128–14138. (e) Oxley, D. S.; Walters, R. W.; Copenhafer, J. E.; Meyer, T. Y.; Petoud, S.; Edenborn, H. M. *Inorg. Chem.* **2009**, *48*, 6332–6334. (f) Wild, A.; Winter, A.; Schlütter, F.; Schubert, U. S. *Chem. Soc. Rev.* **2011**, *40*, 1459–1511.

(4) (a) Chen, X.-Y.; Yang, X.; Holliday, B. J. *J. Am. Chem. Soc.* **2008**, *130*, 1546–1547. (b) Liu, B.; Bao, Y.; Du, F.; Wang, H.; Tian, J.; Bai, R. *Chem. Commun.* **2011**, *47*, 1731–1733.

(5) Borkovec, M.; Hamacek, J.; Piguet, C. *Dalton Trans.* **2004**, 4096–4105.

(6) van der Ende, B. M.; Aarts, L.; Meijerink, A. *Phys. Chem. Chem. Phys.* **2009**, *11*, 11081–11095.

(7) (a) Auzel, F. *Chem. Rev.* **2004**, *104*, 139–173. (b) Wang, F.; Liu, X. *Chem. Soc. Rev.* **2009**, *38*, 976–989.

(8) (a) Koullourou, T.; Natrajan, L. S.; Bhavsar, H.; Pope, S. J. A.; Feng, J.; Narvainen, J.; Shaw, R.; Scales, E.; Kauppinen, R.; Kenwright, A. M.; Faulkner, S. *J. Am. Chem. Soc.* **2008**, *130*, 2178–2179. (b) Nonat, A. M.; Quinn, S. J.; Gunnlaugsson, T. *Inorg. Chem.* **2009**, *48*, 4646–4648. (c) Andrews, M.; Amoroso, A. J.; Harding, L. P.; Pope, S. J. *Dalton Trans.* **2010**, *39*, 3407–3411. (d) Tallec, G.; Imbert, D.; Fries, P. H.; Mazzanti, M. *Dalton Trans.* **2010**, *39*, 9490–9492. (e) Lewis, D. J.; Glover, P. B.; Solomons, M. C.; Pikramenou, Z. *J. Am. Chem. Soc.* **2011**, *133*, 1033–1043.

(9) (a) Reisfeld, R.; Jørgensen, C. K. *Lasers and Excited States or Rare Earths*; Springer-Verlag: Berlin, 1977. (b) Shen, Y.; Riedener, T.; Bray, K. L. *Phys. Rev. B* **2000**, *61*, 11460–11471. (c) Kuriki, K.; Koike, Y.; Okamoto, Y. *Chem. Rev.* **2002**, *102*, 2347–2356.

(10) (a) Riis-Johannessen, T.; Dalla Favera, N.; Todorova, T. K.; Huber, S. M.; Gagliardi, L.; Piguet, C. *Chem.—Eur. J.* **2009**, *15*, 12702–12718. (b) Dalla Favera, N.; Kiehne, U.; Bunzen, J.; Hyteballe, S.; Lützen, A.; Piguet, C. *Angew. Chem., Int. Ed.* **2010**, *49*, 125–128.

(11) (a) Bünzli, J.-C. G. *Lanthanide Probes in Life, Chemical and Earth Sciences*; Elsevier: Amsterdam, 1989; Chap. 7. (b) Parker, D.; Dickins, R. S.; Puschmann, H.; Crossland, C.; Howard, J. A. K. *Chem. Rev.* **2002**, *102*, 1977–2010. (c) Comby, S.; Bünzli, J.-C. G. In *Handbook on the Physics and Chemistry of Rare Earths*; Gschneidner, K. A., Jr., Bünzli, J.-C. G., Pecharsky, V. K., Eds.; Elsevier Science: Amsterdam, 2007; Vol. 37, pp 217−470. (d) dos Santos, C. M. G.; Harte, A. J.; Quinn, S. J.; Gunnlaugsson, T. *Coord. Chem. Rev.* **2008**, *252*, 2512–2527.

(12) Lemonnier, J.-F.; Guénée, L.; Bernardinelli, G.; Vigier, J.-F.; Bocquet, B.; Piguet, C. *Inorg. Chem.* **2010**, *49*, 1252–1265.

(13) A drastic anti-cooperative chelate factor of γ = EM$_1$ EM$_2$/(EM)^2 = $10^{-5.6}$ (compared with γ = 1 for a statistical behavior) prevents the detection of the usual saturated macrobicyclic triple-stranded helicate $[\mathrm{Ln_2}(\mathbf{L3})_3]^{6+}$, while the macromonocyclic double-stranded helicate $[\mathrm{Ln_2}(\mathbf{L3})_2]^{6+}$ suffers from the operation of a very low effective molarity, EM$_1$ = $10^{-7(1)}$ M. Ercolani, G.; Schiaffino, L. *Angew. Chem., Int. Ed.* **2011**, *50*, 1762–1768.

(14) (a) Sabbatini, N.; Guardigli, M.; Manet, I. In *Handbook on the Physics and Chemistry of Rare Earths*; Gschneidner, K. A., Jr., Eyring, L., Eds.; Elsevier Science: Amsterdam, 1996; Vol. 23, pp 69–120. (b) Moore, E. G.; Samuel, A. P. S.; Raymond, K. N. *Acc. Chem. Res.* **2009**, *42*, 542–552. (c) Petoud, S. *Chimia* **2009**, *63*, 745–752.

(15) Weissman, S. I. *J. Chem. Phys.* **1942**, *10*, 214–217.

(16) (a) Beeby, A.; Faulkner, S.; Parker, D. A.; Williams, J. A. G. *J. Chem. Soc., Perkin Trans. 2* **2001**, 1268–1273. (b) Dossing, A. *Eur. J. Inorg. Chem.* **2005**, 1425–1434. (c) Faulkner, S.; Pope, S. J. A.; Burton-Pye, B. P. *Appl. Spectrosc. Rev.* **2005**, *40*, 1–35. (d) Ward, M. D. *Coord. Chem. Rev.* **2010**, *254*, 2634–2642.

(17) (a) Malta, O. L. *J. Lumin.* **1997**, *71*, 229–236. (b) Yang, C.-Y.; Fu, L.-M.; Wang, Y.; Zhang, J.-P.; Wong, W.-T.; Ai, X.-C.; Qiao, Y.-F.; Zou, B.-S.; Gui, L.-L. *Angew. Chem., Int. Ed.* **2004**, *43*, 5010–5013. (c) Lo, W.-K.; Wong, W. K.; Wong, W.-Y.; Guo, J.; Yeung, K.-T.; Cheng, Y.-K.; Yang, X.; Jones, R. A. *Inorg. Chem.* **2006**, *45*, 9315–9325. (d) Perry, W. S.; Pope, S. J. A.; Allain, C.; Coe, B. J.; Kenwright, A. M.; Faulkner, S. *Dalton Trans.* **2010**, *39*, 10974–10983. (e) Ha-Thi, M.-H.; Delaire, J. A.; Michelet, V.; Leray, I. *J. Phys. Chem. A* **2010**, *114*, 3264–3269.

(18) (a) Bünzli, J.-C. G.; Chauvin, A.-S.; Kim, H. K.; Deiters, E.; Eliseeva, S. V. *Coord. Chem. Rev.* **2010**, *254*, 2623–2633. (b) Wagenknecht, P. S.; Ford, P. C. *Coord. Chem. Rev.* **2011**, *255*, 591–616.

(19) Since the two $[\mathrm{Ln(hfac)_3}]$-accepting units are related by symmetry operations in $[\mathrm{Ln_2}(\mathbf{L}\boldsymbol{k})(\mathrm{hfac})_6]$, Neumann's principle implies that the kinetic rate constants for the two bound metals are identical. (a) Nye, J. F. *Physical Properties of Crystals*; Clarendon Press: Oxford, 1985; p 20. (b) Haussühl, S. *Kristallphysik*; Physic-Verlag: Weinheim, 1983; p 13.

(20) All possible internal conversion processes are omitted for clarity, which justifies that the intersystem crossing and energy-transfer processes are represented by non-horizontal arrows.Henderson, B.; Imbusch, G. F. *Optical Spectroscopy of Inorganic Solids*; Clarendon Press: Oxford, 1989.

(21) (a) Sabbatini, N.; Guardigli, M.; Lehn, J.-M. *Coord. Chem. Rev.* **1993**, *123*, 201–228. (b) Petoud, S.; Bünzli, J.-C. G.; Glanzman, T.; Piguet, C.; Xiang, Q.; Thummel, R. *J. Luminesc.* **1999**, *82*, 69–79.

(22) (a) Carnall, W. T. In *Handbook on the Physics and Chemistry of Rare Earths*; Gschneidner, K. A., Jr., Eyring, L., Eds.; North-Holland Publishing Co.: Amsterdam, 1979; Vol. 3, pp 171–208. (b) Aebischer, A.; Gumy, F.; Bünzli, J.-C. G. *Phys. Chem. Chem. Phys.* **2009**, *11*, 1346–1353 and references therein.

(23) Görller-Walrand, C.; Binnemans, K. In *Handbook on the Physics and Chemistry of Rare Earths*; Gschneidner, K. A., Jr., Eyring, L., Eds.; Elsevier Science: Amsterdam, 1998; Vol. 25, pp 101–264.

(24) Reinhard, C.; Güdel, H. U. *Inorg. Chem.* **2002**, *41*, 1048–1055 and references therein.

(25) de Sa, G. F.; Malta, O. L.; de Mello Donega, C.; Simas, A. M.; Longo, R. L.; Santa-Cruz, P. A.; da Silva, E. F., Jr *Coord. Chem. Rev.* **2000**, *196*, 165–195.

(26) Latva, M.; Takalo, H.; Mukkala, V.-M.; Matachescu, C.; Rodriguez-Ubis, J. C.; Kankare, J. *J. Lumin.* **1997**, *75*, 149–169. (b) D'Aléo, A.; Xu, J.; Moore, E. G.; Jocher, C. J.; Raymond, K. N. *Inorg. Chem.* **2008**, *47*, 6109–6111. (c) Samuel, A. P. S.; Xu, J.; Raymond, K. N. *Inorg. Chem.* **2009**, *48*, 687–698. (d) Shavaleev, N. M.; Eliseeva, S. V.; Scopelliti, R.; Bünzli, J.-C. G. *Inorg. Chem.* **2010**, *49*, 3929–3936.

(27) (a) Tobita, S.; Arakawa, M.; Tanaka, I. *J. Phys. Chem.* **1984**, *88*, 2697–2702. (b) Tobita, S.; Arakawa, M.; Tanaka, I. *J. Phys. Chem.* **1985**, *89*, 5649–5654.

(28) Steemers, F. J.; Verboom, W.; Reinhoudt, D. N.; van der Tol, E. B.; Verhoeven, J. W. *J. Am. Chem. Soc.* **1995**, *117*, 9408–9414.

(29) Yamaguchi, Y.; Matsubara, Y.; Ochi, T.; Wakamiya, T.; Yoshida, Z.-I. *J. Am. Chem. Soc.* **2008**, *130*, 13867–13869. The conjugation length $A_\pi = \ln(k_r^{\,F}/k_{nr}^{\,F})$ has no unit and is proportional to the difference $\Delta\mu$ between the S$_1$ state dipole moment (μ_1) and the S$_0$ state dipole moment (μ_0). $\Delta\mu$ can be estimated by using the Lippert–Mataga equation, $\Delta\mu = (\mu_1 - \mu_0) \propto ((\tilde{\nu}_a - \tilde{\nu}_f)a^3)^{1/2}$, in which $\tilde{\nu}_a - \tilde{\nu}_f$ corresponds to the difference in energy between the absorption and fluorescence peaks and a is the molecular radius.

(30) $26° < \alpha < 34°$ were found in the crystal structure of $\mathbf{L3}\cdot 3\mathrm{CHCl_3}$.[12]

(31) Crowther, G. P.; Sundberg, R. J.; Sarpeshkar, A. M. *J. Org. Chem.* **1984**, *49*, 4657–4663.

(32) Iovine, P. M.; Kellett, M. A.; Redmore, N. P.; Therien, M. J. *J. Am. Chem. Soc.* **2000**, *122*, 8717–8727.

(33) For **L4**, H15 appears as a pseudo-triplet because of its scalar coupling with the two fluorine atoms with $J_{\mathrm{H\text{-}F}}^{\ 3} \simeq J_{\mathrm{H\text{-}F}}^{\ 4}$ = 8.6 Hz.Clerc, T.; Pretsch, E. *Kernresosonanz-Spectroskopie*; Akademische Verlagsgesellshaft: Frankfurt, 1973; p 114.

(34) Lunazzi, L.; Mazzanti, A.; Minzoni, M.; Anderson, J. E. *Org. Lett.* **2005**, *7*, 1291–1294.

(35) The rate of Einstein spontaneous emission in the dipole approximation is given by $k_r = ((\omega^3 n|\mu_{12}|^2)/(3\pi\varepsilon_0\hbar c^3))$, where ω is the emission frequency, n is the index of refraction, μ_{12} is the transition dipole moment, ε_0 is the vacuum permittivity, $\hbar$ is the reduced Planck constant, and c is the vacuum speed of light. (a) Einstein, A. *Phys. Z.* **1917**, *18*, 121. (b) Pais, A. *Rev. Mod. Phys.* **1977**, *49*, 925–938. (c) Valeur, B. *Molecular Fluorescence*; Wiley-VCH: Weinheim, 2002.

(36) Yuasa, J.; Ohno, T.; Miyata, K.; Tsumatori, H.; Hasegawa, Y.; Kawai, T. *J. Am. Chem. Soc.* **2011**, *133*, 9892–9902.

(37) Meech, S. R.; Phillips, D. C. *J. Photochem.* **1983**, *23*, 193–217.

(38) (a) Evans, W. J.; Giarikos, D. G.; Johnston, M. A.; Greci, M. A.; Ziller, J. W. *J. Chem. Soc., Dalton Trans.* **2002**, 520–526. (b) Malandrino, G.; Lo Nigro, R.; Fragalà, I. L.; Benelli, C. *Eur. J. Inorg. Chem.* **2004**, 500–509.

(39) Binnemans, K. In *Handbook on the Physics and Chemistry of Rare Earths*; Gschneidner, K. A., Jr., Bünzli, J. C. G., Pecharsky, V. K., Eds.; Elsevier North Holland: Amsterdam, 2005; Vol. 35, pp 107–272.

(40) Escande, A.; Guénée, L.; Buchwalder, K.-L.; Piguet, C. *Inorg. Chem.* **2009**, *48*, 1132–1147.

(41) (a) Brown, I. D.; Altermatt, D. *Acta Crystallogr. B* **1985**, *41*, 244–247. (b) Breese, N. E.; O'Keeffe, M. *Acta Crystallogr. B* **1991**, *47*, 192–197. (c) Brown, I. D. *Acta Crystallogr. B* **1992**, *48*, 553–572. (d) Brown, I. D. *The Chemical Bond in Inorganic Chemistry*; Oxford University Press: Oxford, 2002. (e) Trzesowska, I. D.; Kruszynski, R.; Bartczak, T. J. *Acta Crystallogr. B* **2004**, *60*, 174–178. (f) Trzesowska, A.; Kruszynski, R.; Bartczak, T. J. *Acta Crystallogr. B* **2005**, *61*, 429–434. (g) Zocchi, F. *J. Mol. Struct.* **2007**, *825–846*, 73–78. (h) Brown, I. D. *Chem. Rev.* **2009**, *109*, 6858–6919.

(42) Dalla Favera, N.; Guénée, L.; Bernadinelli, G.; Piguet, C. *Dalton Trans.* **2009**, 7625–7638.

(43) Carnall, W. T.; Fields, P. R.; Rajnak, K. *J. Chem. Phys.* **1968**, *49*, 4443–4446.

(44) (a) Davydof, A. S. *Theory of Absorption of Light in Molecular Crystals*; Ukrainian Academy of Sciences: Kiev, 1951. (b) Kasha, M.; Oppenheimer, M. *Theory of Molecular Excitons*; McGraw-Hill Book Co. Inc.: New York, 1962. (c) Telfer, S. G.; McLean, T.; Waterland, M. R. *Dalton Trans.* **2011**, *40*, 3097–3108.

(45) (a) Nakamoto, K. *J. Phys. Chem.* **1960**, *64*, 1420–1425. (b) Piguet, C.; Bocquet, B.; Müller, E.; Williams, A. F. *Helv. Chim. Acta* **1989**, *72*, 323–337.

(46) The π-delocalized didentate hfac$^-$ counter-anions also possess ligand-centered excited states which may contribute to the global sensitization process in $[\mathrm{Ln_2}(\mathbf{L}\boldsymbol{k})(\mathrm{hfac})_6]$. This assumption is demonstrated by the absorption spectrum of the starting metallic complex $[\mathrm{Gd(hfac)_3(diglyme)}]$, which exhibits an intense absorption band centered at 33060 cm^{-1} (ε = 33 300 M^{-1} cm^{-1}, Figures 8 and S11) that is assigned to the hfac-centered $\pi \rightarrow \pi^*$ transitions. Irradiation of $[\mathrm{Gd(hfac)_3(diglyme)}]$ at $\bar{\nu}_{\mathrm{exc}}$ = 32 790 cm^{-1} produces both faint fluorescence ($E(^1\pi\pi^*)$ = 26 320 cm^{-1}, Figure S12a) and weak

phosphorescence ($E(^3\pi\pi^*)$ = 21 800 cm^{-1}, $\tau_L(P)$ = 270(20) μs at 293 K, Figure S12b).

(47) Equation 11 holds when the intersystem crossing process is the only significant additional perturbation of the $^1\pi\pi^*$ deactivation pathway produced by the complexation of Gd(III).Torelli, S.; Imbert, D.; Cantuel, M.; Bernardinelli, G.; Delahaye, S.; Hauser, A.; Bünzli, J.-C. G.; Piguet, C. *Chem.—Eur. J.* **2005**, *11*, 3228–3242.

(48) Carnall, W. T.; Fields, P. R.; Rajnak, K. *J. Chem. Phys.* **1968**, *49*, 4450–4455.

(49) Skoog, D. A.; West, D. M.; Holler, F. J.; Crouch, S. R. *Fundamentals of Analytical Chemistry*, 8th ed.; Brooks Cole: 2003; Chap. 3.

(50) Altomare, A.; Burla, M. C.; Camalli, M.; Cascarano, G.; Giacovazzo, C.; Guagliardi, A.; Moliterni, G.; Polidori, G.; Spagna, R. *J. Appl. Crystallogr.* **1999**, *32*, 115–119.

(51) Sheldrick, G. M. *SHELXL97*, Program for the Solution and Refinement of Crystal Structures; University of Göttingen, Germany, 1997.

(52) Johnson, C. K. *ORTEP II*, Report ORNL-5138; Oak Ridge National Laboratory: Oak Ridge, TN, 1976.

(53) Casida, M. E. In *Recent Developments and Applications of Modern Density Functional Theory*, Seminario, J. M., Ed.; Elsevier: Amsterdam, 1996; pp 391−439.

(54) *TURBOMOLE*, V6.1 2009; University of Karlsruhe and Forschungszentrum Karlsruhe GmbH, 1989−2007; TURBOMOLE GmbH, since 2007; available from http://www.turbomole.com.

(55) Perdew, J. P.; Burke, K.; Ernzerhof, M. *Phys. Rev. Lett.* **1996**, *77*, 3865–3868.